Universiteit Utrecht

Faculty of Science, Utrecht University
Institute for Subatomic Physics

Event shape and multiplicity dependence of the jet peak in pp collisions at $\sqrt{s_{\mathrm{NN}}} = 13$ TeV with ALICE

Bachelor Thesis

Iris J. Keizer

Physics and Astronomy

Supervisor:

Dr. Panos Christakoglou
Institute for Subatomic Physics at Utrecht University
Dutch National Institute for Subatomic Physics (NIKHEF)

June 12, 2019

Abstract

Collisions between heavy ions create the right conditions for the formation of the quark-gluon plasma (QGP). Recently, proton-proton (pp) collisions at the Large Hadron Collider (LHC) produced results similar to those obtained from lead-lead (Pb-Pb) collisions. This raises the question whether the QGP is also created in pp collisions. An indication of the presence of the QGP is the observation of jet quenching. In order to find out if the QGP is produced in pp collisions this thesis focusses on the study of jets. The angular correlations between charged particles is studied as a function of multiplicity (N_{ch}) and transverse momentum (p_{T}). The jet shape is examined by calculating the width of the near-side peak and the yield for both the near- and away-side peak. This analysis will be done for inclusive, low, and mid sphericity. Data from pp collisions at center-of-mass energy $\sqrt{s_{NN}} = 13$ TeV from the ALICE collaboration is used. For lower multiplicity classes, a broadening of the peak in the direction of both $\Delta\phi$ and $\Delta\eta$ is observed. The increase of the width is strongest in the $\Delta\eta$ direction. This dependence is prominent for momentum ranges: $p_{\mathrm{T,trig}} = 2.0 - 6.0$ GeV/c and $p_{\mathrm{T,assoc}} = 0.2 - 2.0$ GeV/c, $p_{\mathrm{T,trig}} = 6.0 - 15.0$ GeV/c and $p_{\mathrm{T,assoc}} = 0.2 - 2.0$ GeV/c and $p_{\mathrm{T,trig}} = 2.0 - 6.0$ GeV/c and $p_{\mathrm{T,assoc}} = 2.0 - 6.0$ GeV/c. The results of the $\sqrt{s_{NN}} = 13$ TeV analysis will be compared to a similar study at center-of-mass energy $\sqrt{s_{NN}} = 5$ TeV. The results of these two studies agree well.

Contents

1 Introduction

Elementary particles are the building blocks of all matter and antimatter. They are named quarks, leptons and gauge bosons and they're classified in the Standard Model of particle physics. The observed interactions between these particles are the electromagnetic, weak and strong interaction, which are also part of the Standard Model. The strong nuclear force is described by the theory of quantum chromodynamics (QCD).

The strong interaction between two quarks is mediated by a gluon. Quarks and gluons only exist confined in hadrons which are particles such as protons and neutrons. However, QCD predicts that at extreme energy densities and temperatures these hadrons can "melt"and deconfined matter of quarks and gluons can exist. This deconfined matter is called the quark-gluon plasma (QGP). [8]

At the beginning of time, the universe originated in a "Big Bang"which was a fireball of almost infinite temperature and density. Some 10 picoseconds after the Big Bang, lasting for 10 microseconds, the universe is thought to have taken the form of the QGP. [11] [9]

In collisions between heavy ions at particle accelerators like the Large Hadron Collider (LHC) in Geneva the QGP can be created. The particles are accelerated at very high velocities such that their momentum allows for a collision energy that's high enough to form the plasma. One of the four main experiments at the LHC is A Large Ion Collider Experiment (ALICE). ALICE's purpose is to study the properties of the QGP.

Recent collisions between smaller systems - such as between two protons - show results that indicate the formation of the QGP in these smaller systems [3]. Experimental observations obtained from pp-collisions are similar to results from experiments using heavy-ion collisions. One might wonder whether these similarities between the results of small and large collision systems are due to the same underlying physical mechanisms. The collisions between smaller systems are thus an interesting research topic

In this thesis we focus on pp collisions at $\sqrt{s_{NN}} = 13$ TeV. The width and yield of the near-side peak of the events are calculated using the two-particle angular correlation technique. The analysis is done for inclusive sphericity as well as the low-, mid- and high-sphericity event shapes. The results will be presented as a function of several multiplicity classes as well as several transverse momentum ranges. They will be compared to a similar study at 5TeV to study the effect of the energy on the peak shape.

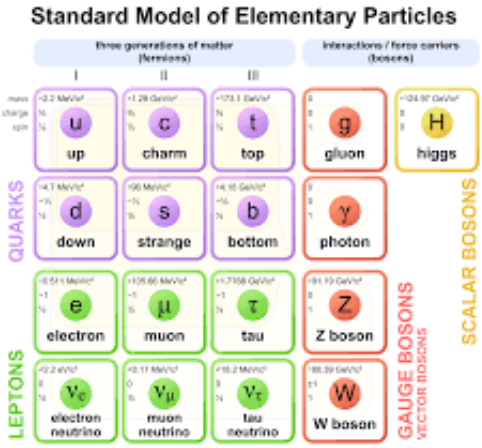

Figure 1: An overview of the elementary particles contained in the Standard Model.

2 Theoretical and experimental background

2.1 Quark-gluon plasma

The Standard Model consists of fermions and gauge bosons. The fermions are divided into quarks and leptons. These quarks exist in three colors - red, green and blue - while all naturally occuring particles are colorless. Furthermore, gauge bosons are the particles that mediate the interactions between matter and gluons are the mediator of the strong force. Moreover, these gluons carry the color that is transferred in an interaction between quarks. A gluon carries both a positive and negative unit of color charge. Quarks and gluons are referred to as partons.

The theory that describes the strong nuclear interaction is called quantum chromodynamics (QCD). This theory explains how the world of quarks and gluons works. Since matter does not have color charge, quarks and gluons are confined in hadrons. They're bound together by the strong interaction. QCD describes a feature named asymptotic freedom. The phenomenon that the strong interaction becomes weaker at larger energy scales and shorter length scales. This prevents the separation of individual quarks at earthlike circumstances. However, at extreme temperatures and energy densities, it also predicts the existence of a matter of deconfined quarks and gluons, known as the quark-gluon plasma (QGP). The theory of QCD describes high-p_{T} partons perturbatively while low-p_{T} partons are described using QCD-inspired phenomenological models.

During the first few microseconds after the Big Bang the universe was filled with the quark-gluon plasma, an astonishingly hot and dense soup made of quarks, antiquarks and gluons moving at nearly the speed of light. The universe only stayed in this state for about 10 microseconds. Then the universe cooled down below the critical point and hadronic matter started to exist.[11][14]

2.2 Particle accelerators

Particle accelerators are important for the study of fundamental particles. These accelerators discover new particles and enable researchers to study their properties. Currently, the most powerful accelerator is the Large Hadron Collider (LHC) at the CERN laboratory near Geneva. The LHC is a collaboration of over ten thousand scientists from different universities and laboratories all over the world. The particle collider lies in a circular tunnel with a circumference of 27 kilometers at a depth of 175 meters. After several updates, the LHC now collides particles at an energy of 6.5 TeV per proton, reaching a world record collision energy of 13 TeV.

The LHC contains seven detectors situated in caverns at intersection points. The four main experiments are ALICE, ATLAS, LHCb and CMS. The other three experiments are much smaller. The ATLAS and CMS experiments were involved in the discovery of the Higgs boson. Where ATLAS and CMS are particle detectors with a general purpose ALICE and LHCb have more specific roles. During the Big Bang equal amounts of matter and antimatter were created. Nowadays, antimatter seems to be “missing”, LHCb investigates what happened to this antimatter. ALICE, the detector used for this thesis, studies the properties of the quark-gluon plasma.[13][15]

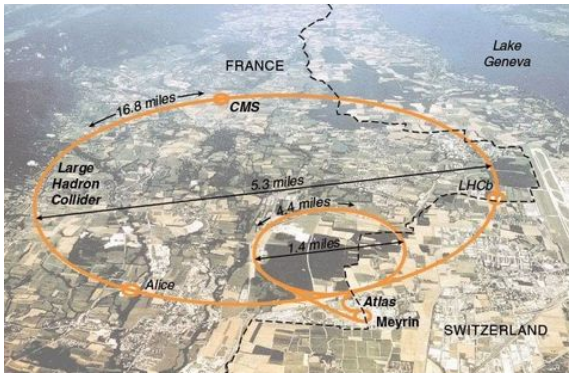

(a) Aerial view of the LHC

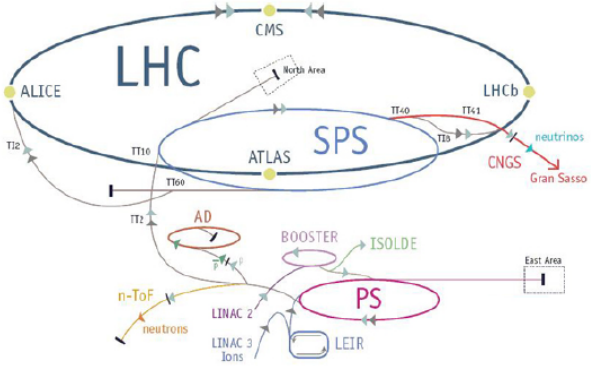

(b) Schematic overview of the LHC. The figure is reproduced from [15].

Figure 2

2.3 ALICE

ALICE studies the properties of the QGP by creating extreme temperatures and energy densities in collisions between hadrons. The ALICE collaboration has created the QGP in ultrarelativistic collisions of heavy ions (Pb-Pb). Recent results of p-Pb and p-p collisions show similarities to the Pb-Pb collisions. This indicates that the QGP might also be formed in these smaller systems and motivates the study of pp collisions.

ALICE consists of 18 subdetectors that are optimized for specific tasks. The detectors are situated around the interaction region. These detectors identify the particles by the characteristic signatures they leave when interacting with the material. Also the trajectories of the particles are reconstructed and their energy is measured. The collision particles will first go through a tracking system, then an electromagnetic calorimeter and finally a muon system.

The detectors mainly used for this study are the Inner Tracking System (ITS), the Time Projection Chamber (TPC) and the V0 detectors. Short-living heavy particles are produced during collisions, the ITS measures the locations where these particles decay. The ITS consists of six layers, located from 3.9 cm up to 43 cm from the beam axis. The two layers closest to the beam axis are the Silicon Pixel Detector (SPD) which determines the location of the collision, the primary vertex.

The ITS is surrounded by the TPC, the main particle path tracking detector. The TPC is a cylindrical volume of 90 m^3 filled with Ne-CO_2 gas. TPC consists of endplates and a central membrane, held at a potential difference of $\Delta V \sim 100$ kV relative to each other. Charged particles that travel through the gas ionize the molecules they encounter. The freed electrons drift towards the endplates due to the electric field within the TPC. Thereby, they create a projection of their trajectory on the endplates. The TPC also measures the momentum and pseudorapidity of the particles.

The V0 detector is used to estimate the centrality of an event. It consists of two disks, scintillator counters V0A and V0C, on both sides of the detector, at $z = 3.4$ m and $z = -0.9$ m. The disks detect the number of particles crossing their sensitive area which scales directly with the generated number of primary particles and thus with the centrality of the event. For heavy-ion collisions both the V0A and V0C are used. However, in pp collisions and thus in this thesis only the V0A is used.[13][1][15]

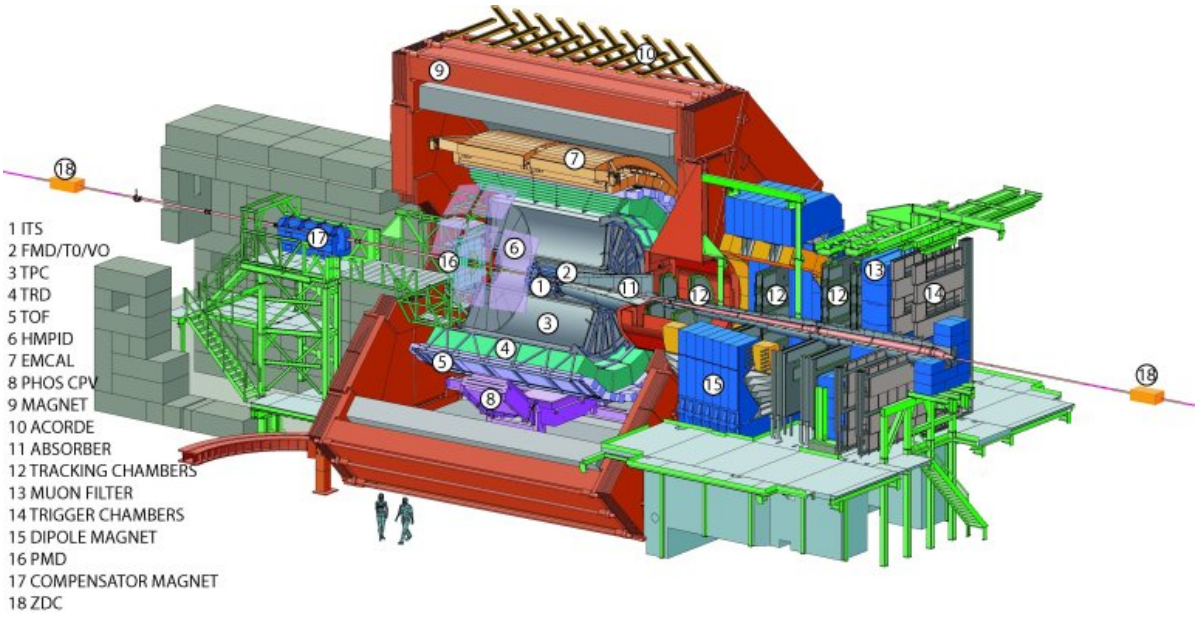

Figure 3: Schematic illustration of the ALICE detector, showing the various subdetectors. The figure is taken from [7]

2.4 Jet quenching

In ultrarelativistic collisions between particles, high energy quarks are created. These quarks head off in opposite direction (back-to-back). Since deconfined quarks cannot exist, another pair of quarks is created. Together with the original quark they form a new hadron, a process known as hadronization. The hadrons often decay into more stable lighter particles. The result is a back-to-back jet of particles whereof the resulting hadrons can directly be detected.

At the LHC, the temperature is high enough to melt the nuclei created in the collision and form the QGP. The high-p_{T} partons that result in the described particle jets transverse the QGP consisting of low-p_{T} partons. The partons interact strongly with the medium through medium-induced gluon radiation (bremstrahlung) and collisions with partons in the medium. These interactions result in a reduction of the energy of the partons and thus modify the produced jets. This process is called jet quenching and can be studied using experimental measurements of detected hadrons, two particle correlations and jet reconstruction.

A parton loses energy through QGP-induced gluon radiation. The color charge of the parton interacts with the color charges of the QGP. This results in the emition of a bremsstrahlung gluon. This emitted gluon itself carries color charge and again interacts with the color charges in the QGP. [10][11]

2.5 Two-particle angular correlation

The method used to study the jets is the two-particle angular correlation technique. Hard partons are produced in pairs separated by 180° in the transverse plane, i.e. the plane perpendicular to the beam axis, which is the z-axis. These partons result in back-to-back jets when they hadronize. A high-p_T particle is selected to define the coordinate system, this particle is called the trigger particle. Due to the high-p_T of the trigger particle it is a good approximation of the jet axis it arose from. As a next step the angular differences between the trigger particle and the other particles, referred to as associated particles, is measured using the difference in azimuthal angle($\Delta\phi = \phi_{\mathrm{trig}} - \phi_{\mathrm{assoc}}$) and the difference in pseudorapidity ($\Delta\eta = \eta_{\mathrm{trig}} - \eta_{\mathrm{assoc}}$).

The pseudorapidity η is a coordinate that describes the angle of a particle relative to the beam axis. The azimuthal angle ϕ is measured between the particle path and the x-axis, which points from the beam towards

the centre of the LHC. A schematic view can be found in figure 4. The coordinates can be calculated using:

$$\phi = \arctan\frac{y}{x} \quad (1) \qquad \eta = -\ln\tan\frac{\theta}{2}. \quad (2)$$

Where θ is the angle with respect to the beam axis, measured as:

$$\theta = \arccos\frac{z}{\sqrt{x^2+y^2+z^2}}. \quad (3)$$

Once $\Delta\phi$ and $\Delta\eta$ have been calculated the associated particle distribution can be determined:

$$\frac{1}{N_{\text{trig}}}\frac{d^2}{d\Delta\phi d\Delta\eta}, \quad (4)$$

where N_{trig} is the number of trigger particles in the analyzed sample. Dividing by N_{trig} ensures that the analysis is independent of sample size. Since this distribution also includes pair acceptance and pair efficiency the mixed-event technique is used. The particle yield distribution from one event is associated with the trigger particles from another (uncorrelated) event. This distribution is sensitive to the pair acceptance and pair efficience but does not contain pair correlations by construction. The associated yield distribution, containing the distribution associated with trigger particles from the same event, is divided by the mixed event distribution to generate the physical signal that is used for analyzing.[15]

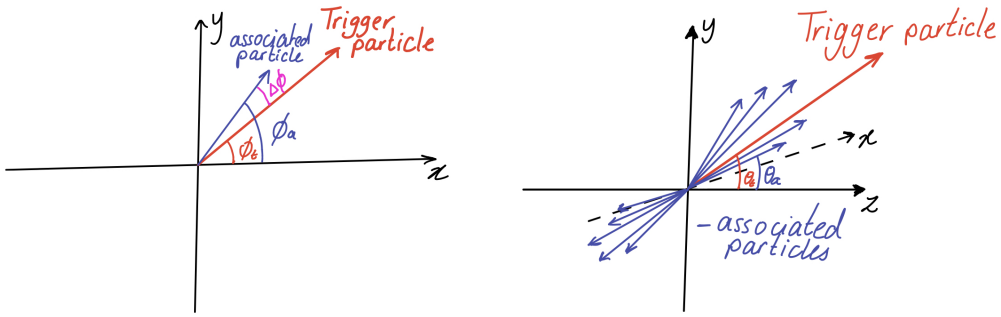

Figure 4: Schematic diagram showing the identification of a trigger particle in a pp collision and its use to determine θ and ϕ.

Since the signal is primarily caused by back-to-back jets, certain structures in the shape of the signal can be expected. At $\Delta\phi = \Delta\eta = 0$ a peak-shaped structure can be expected, called the near-side peak. The peak-shape is caused by the small difference in both angles between the trigger particle and the associated particle belonging to the same jet. At low p_{T}, resonance decays as well as femtoscopic correlations also contribute to the near-side peak. Another peak shape can be expected at $\Delta\eta = 0$ and $\Delta\phi = \pi$, called the away-side ridge. The away-side ridge is caused by the parton that traversed the QGP in opposite direction compared to the parton where the trigger particle originated from. These associated particles have $\Delta\eta \approx 0$ and $\Delta\phi \approx \pi$.[5][15][11]

Also, two ridge-shaped structures elongated along $\Delta\eta$ and at $\Delta\phi = 0$ (near-side ridge) and $\Delta\phi = \pi$ (away-side ridge) are often observed. These structures originate from the collective motion or flow of the low-p_T partons contained in the QGP. In a non-central heavy-ion collision the overlap region of the two-colliding nuclei is spatially deformed, having an almond instead of circular shape. This deformation is illustrated in the left panel of figure 5. Rescattering processes among the produced particles transfer this spatial deformation onto momentum space. Particles produced in the beam direction carry more momentum than particles produced in the transverse plane. At similar momentum, the particle yield is therefore enhanced in the direction of

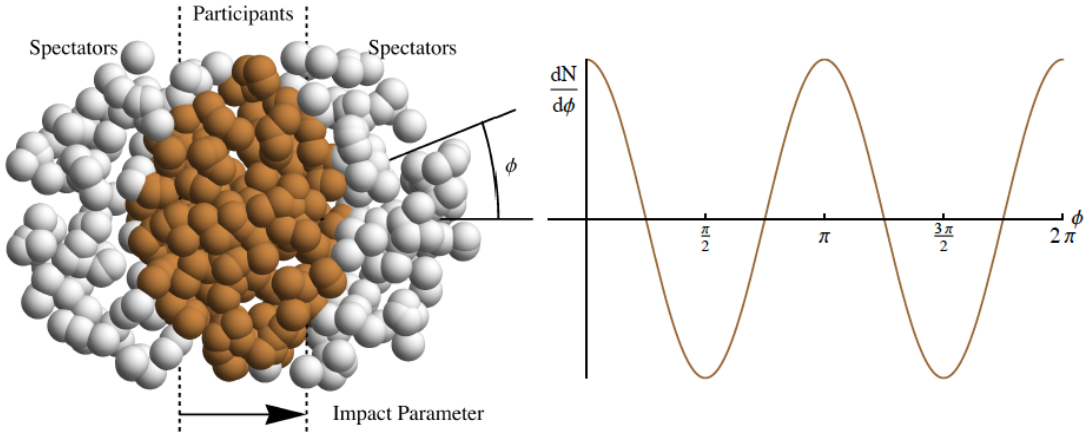

Figure 5: Illustration of a Pb-Pb collision looking at the beam axis. Figure is reproduced from [15]

the impact parameter, this is illustrated in right panel of figure 5 [11][15]

The per-trigger yield is calculated for various centrality ranges which are determined using the charged particle multiplicity N_{ch}. The centrality percentage is calculated by comparing the multiplicity of a given event to the multiplicity distribution of all events. The 10% of all events with the highest multiplicity are referred to as $0-10\%$ central. The lower centrality percentage ranges are thus referred to as having high multiplicity.[10]

In heavy-ion collisions, the away-side peak is observed to dissapear for events with higher multiplicity. The current interpretation for this is that the trigger particle represents a jet moving outward of the QGP, coming only from a thin surface layer of the QGP. The inward-moving partner of the outward-moving jet loses so much energy by traveling through the QGP that they no longer make hadrons that are included in the angular correlation function. This results in the suppression of the away-side peak. An illustration of the effect can be seen in figure 6. However, these jet quenching effects, observed in Pb-Pb collisions, have not been observed in pp collisions. [11][14]

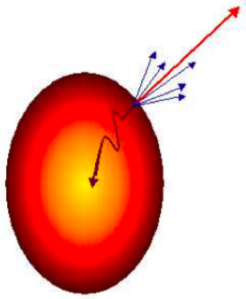

Figure 6: Illustration of outward jet emission from the QGP surface and quenching of the corresponding inward-moving parton by the dense interior. Figure is reproduced from [11]

2.6 Sphericity

At hadron colliders, event shapes are defined in the transverse plane, i.e. the plane perpendicular to the beam axis. The shape of an event can be defined using the transverse sphericity, S_t. The sphericity describes the energy flow based on the momentum tensor. To calculate S_T the transverse momentum matrix $\mathbf{S}$ should be diagonalized using

$$\mathbf{S} = \frac{1}{\sum_i p_{T,i}} \sum_i \frac{1}{p_{T,i}} \begin{pmatrix} p_{x,i}^2 & p_{x,i}p_{y,i} \\ p_{y,i}p_{x,i} & p_{y,i}^2 \end{pmatrix}. \tag{5}$$

Here $p_{T,i}$ is the transverse momentum of the ith particle. The transverse sphericity is defined in terms of the eigenvalues, where $\lambda_1 > \lambda_2$:

$$S_T \equiv \frac{2\lambda_2}{\lambda_1 + \lambda_2} \tag{6}$$

The value of S_T is between 0 for collisions that produce two back-to-back jets (also called jetty events) and 1 for isotropic events. Events with sphericity 0 are referred to as low sphericity, values near 0.5 as mid sphericity and values near 1 as high sphericity.

In pp collisions, a dependence of sphericity on multiplicity as well as the transverse momentum of the trigger particle is observed, as can be seen in figure 7. Events with both higher $p_{\mathrm{T,trig}}$ and multiplicity are seen to be less spherical and thus tend to have a more dijet structure. Also, the total particle yield is expected to increase for more spherical events. [14] [12][2]

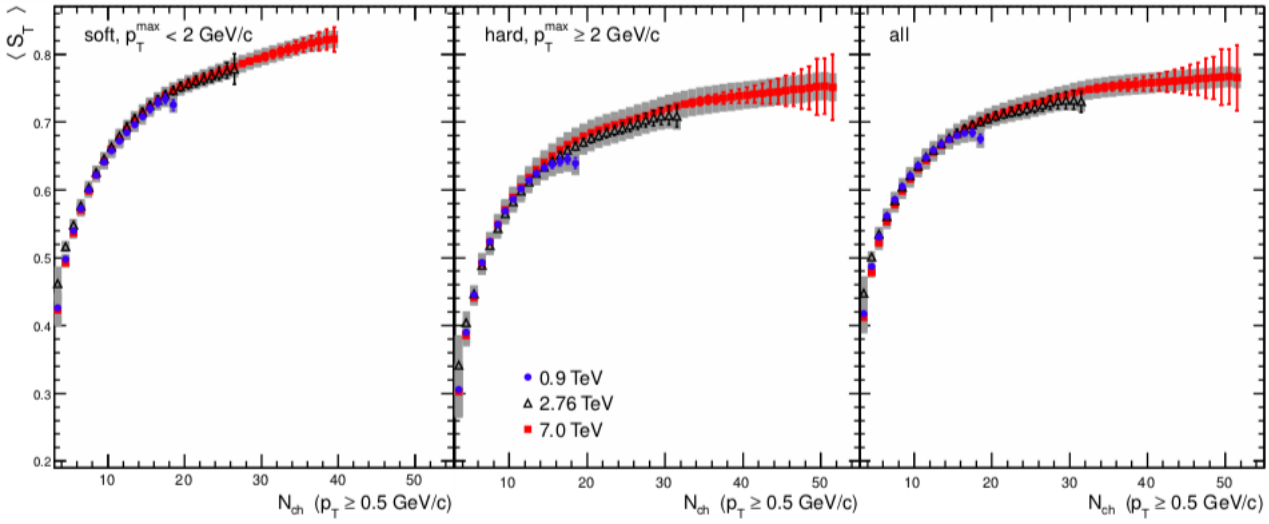

Figure 7: Mean transverse sphericity versus multiplicity for inclusive (right), "hard"(middle) and "soft"(left) pp collisions at $\sqrt{s} = 0.9, 2.76$ and 7 TeV. The statistical errors are displayed as error bars and the systematic uncertainties as the shaded area. Figure is reproduced from [2]

3 Analysis

The multiplicity of the event was determined using the V0A detector. The reconstruction of the event consisted of various steps. First, the primary vertex is determined using the SPD. Thereafter, tracks are reconstructed with signals from the ITS and TPC, where an inward-outward-inward procedure is used. From this, the momentum and pseudorapidity of the track are determined. At last, an improved determination of the primary vertex is made from where of the distant of closest approach (DCA) from each track to the primary vertex is extracted. [6]

3.1 Fitting method

The analysis was performed with data recorded in 2017 at the ALICE detector. During that period the LHC provided pp collisions at a total center of mass energy of $\sqrt{s} = 13$ TeV per nucleon pair. The dataset was analysed using the ROOT framework created by CERN and a code written in C++ that executed the fitting.

Using above tools the per trigger yields of the events were plotted in $\Delta\phi$-$\Delta\eta$ space and also projected in the $\Delta\phi$- and $\Delta\eta$-direction. This was done for multiplicity ranges $0-10\%$ up to $70-80\%$ and for various trigger and associated particle momentum ranges:

$$p_{\mathrm{T,trig}} = 0.2 - 2.0 \text{ GeV/c and } p_{\mathrm{T,assoc}} = 0.2 - 2.0 \text{ GeV/c},$$

$$p_{\mathrm{T,trig}} = 2.0 - 6.0 \text{ GeV/c and } p_{\mathrm{T,assoc}} = 0.2 - 2.0 \text{ GeV/c},$$

$$p_{\mathrm{T,trig}} = 6.0 - 15.0 \text{ GeV/c and } p_{\mathrm{T,assoc}} = 0.2 - 2.0 \text{ GeV/c},$$

$$p_{\mathrm{T,trig}} = 2.0 - 6.0 \text{ GeV/c and } p_{\mathrm{T,assoc}} = 2.0 - 6.0 \text{ GeV/c},$$

$$p_{\mathrm{T,trig}} = 6.0 - 15.0 \text{ GeV/c and } p_{\mathrm{T,assoc}} = 2.0 - 6.0 \text{ GeV/c},$$

$$p_{\mathrm{T,trig}} = 6.0 - 15.0 \text{ GeV/c and } p_{\mathrm{T,assoc}} = 6.0 - 15.0 \text{ GeV/c}.$$

In order to characterize the shape of the peaks, the width and yield are calculated using a χ^2 fitting method. For inclusive sphericity the following fits were used. For the two-dimensional $\Delta\phi - \Delta\eta$ plot the fit function is a combination of a constant and a two-dimensional Gaussian function:

$$F^{\mathrm{Inc}}_{\text{two-dimensional}} = C_1 + C_2 \times e^{-0.5\times(\frac{x-C_3}{C_4})^2} \times e^{-0.5\times(\frac{y-C_5}{C_6})^2} \tag{7}$$

The width in $\Delta\eta$ is than given by the parameter C_4 and the width in $\Delta\phi$ is given by the parameter C_6. The yield of the peak is calculated by integrating:

$$\int_{-3*C_4+C_1}^{3*C_4+C_1} \int_{-3*C_6+C_1}^{3*C_6+C_1} C_1 + C_2 \times e^{-0.5\times(\frac{x-C_3}{C_4})^2} \times e^{-0.5\times(\frac{y-C_5}{C_6})^2} dxdy. \tag{8}$$

After the integration the yield is divided by 2 to make sure that pairs of particles are not counted twice.

For the plots of the projections in $\Delta\phi$ and $\Delta\eta$ the used fit functions are a combination of a constant and a one-dimensional Gaussian function:

$$F_{\text{projection}} = C_1 + C_2 \times e^{-0.5\times(\frac{x-C_3}{C_4})^2} \tag{9}$$

Again, the width is given by C_4. The yield was not calculated using the projections.

For low and mid sphericity a cosine function is added in the direction of $\Delta\phi$. The fit used for the two-dimensional $\Delta\phi - \Delta\eta$ plot is:

$$F^{\mathrm{Low,Mid}}_{\text{two-dimensional}} = C_1 + C_2 \times e^{-0.5\times(\frac{x-C_3}{C_4})^2} \times e^{-0.5\times(\frac{y-C_5}{C_6})^2} + C_7 \times \cos 2y \tag{10}$$

The fit used for the projection of $\Delta\phi$ is:

$$F_{\text{projection}} = C_1 + C_2 \times e^{-0.5\times(\frac{x-C_3}{C_4})^2} + C_5 \times \cos 2x \tag{11}$$

Examples of the fits can be found in figure 8.

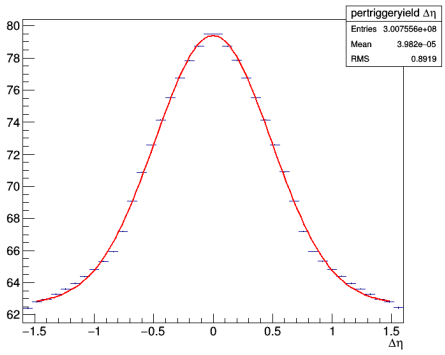

(a) Projection in the $\Delta\eta$ direction and corresponding fit for inclusive sphericity.

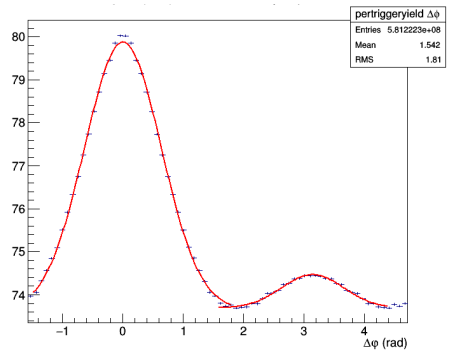

(b) Projection in the $\Delta\phi$ direction and corresponding fit for inclusive sphericity.

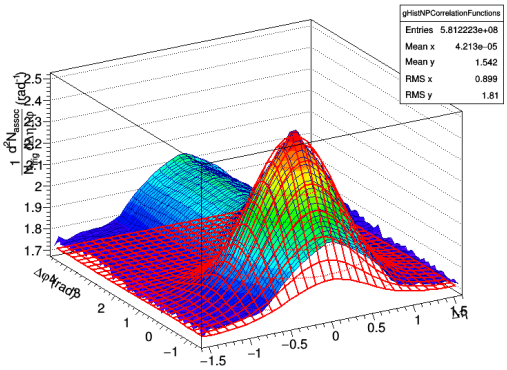

(c) Two-dimensional plot and corresponding near-side fit for inclusive sphericity.

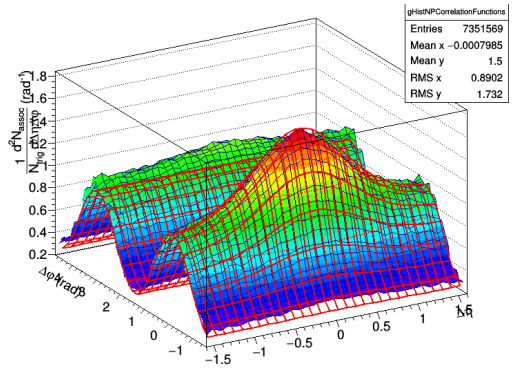

(d) Two-dimensional plot and corresponding near-side fit for low sphericity.

Figure 8: Plots of both the signal and the fit function for multiplicity class $30-40\%$ and momentum ranges $p_{\text{T,trig}} = 0.2-2.0$ GeV/c and $p_{\text{T,assoc}} = 0.2-2.0$ GeV/c.

3.2 Event and track selection

For this analysis, track selection was used in the form of standard cuts on primary tracks. In the TPC, primary charged particles were required to have at least 70 reconstructed space points out of the maximum of 159. For every space point in the TPC and degree of freedom, the average χ^2 of the track fit was required to be below 2. These selections reduce the contribution from tracks that were unlikely to originate from the primary vertex. Further influence of tracks from weak decays or from interaction with the detector material is reduced by only analysing particles within a maximum distance of closest approach between the tracks and the primary vertex in both the traverse plane ($\mathrm{DCA_{xy}} < 2.4$ cm) and the longitudinal direction ($\mathrm{DCA}_z < 3.2$ cm). In the ITS, the tracks were required to have at least two associated ITS-clusters and one hit in either of the two SPD-layers. This selection leads to an efficiency of about 80% for primary tracks at $p_\mathrm{T} > 0.6$ GeV/c and a contamination from secondaries of about 5% at $p_\mathrm{T} = 1$ GeV/c. [4]

3.3 Systematic uncertainties

Systematic uncertainties connected to the analysis are determined by using an alternative track selection. An additional tracking mode was used, relying on the so-called standalone TPC-tracking using the same parameters as described before.
The same analysis is performed using both methods of track selection resulting in two different values, for example X_A and X_B for every observable. Then, the difference is calculated for every multiplicity class and the statistical uncertainty of this difference:

$$\begin{aligned} \Delta X &= X_A - X_B, \\ \sigma\Delta X &= \sqrt{|\sigma X_A^2 - \sigma X_B^2|}. \end{aligned} \tag{12}$$

Since $\Delta X > \sigma\Delta X$ for all values, the values are considered as fully correlated. Thereafter, the differences are plotted and a fit function is contructed for this plot. The systematic uncertainty for the observable is the absolute value of the fit function at the corresponding multiplicity N_ch divided by two, since the values are fully correlated:

$$X_{\text{systematic uncertainty}} = \frac{|\mathrm{Fit}_{\Delta X}(N_\mathrm{ch})|}{2}. \tag{13}$$

4 Results

The results of this thesis are presented per event shape. For every event shape the total yield per trigger particle is shown as a function of pseudorapidity ($\Delta\eta$) and azimuthal ($\Delta\phi$) differences. Also the quantities calculated using the fitting method are shown. These include the width in $\Delta\eta$ and $\Delta\phi$ calculated using the two-dimensional plot as well as the projections in both directions. Also, these include the total yield calculated for the near-side jet peak. In a few cases also the yield for the away-side jet peak are calculated.

4.1 Inclusive sphericity

This paragraph includes the results of the inclusive sphericity analysis. In figure 9 the per-trigger yield for momentum range $p_{\mathrm{T,trig}} = 0.2 - 2.0$ GeV/c and $p_{\mathrm{T,assoc}} = 0.2 - 2.0$ GeV/c, and multiplicity ranges 0-10%, 30-40% and 60-70% are presented. The per-trigger yield figures for higher momentum ranges can be found in appendix A.

In figure 9, the near-side jet peak is clearly present. The jet peak looks symmetric in $\Delta\phi$ and $\Delta\eta$. The shape looks similar to the results of Pb-Pb collisions for $50 - 80\%$ centrality [5]. The away-side jet peak as well as the near- and away-side ridges due to parton flow are not present in 9. Due to the absence of the away-side jet peak, the associated yield could not be calculated.

Unexpectedly, a ridge elongated along $\Delta\phi$ at $\Delta\eta = 0$ is present. This ridge becomes higher for lower multiplicity and becomes smaller, dissapearing quickly, for higher momentum ranges, as can be seen in appendix A. The explanation of this ridge phenomenon goes beyond the purpose of this study. However, the shapes appear to be interesting topics for future research.

In figure 10, the yield and peak shape as a function of momentum and multiplicity are presented. For both the yield and width of the jet peak the results for $p_{\mathrm{T,trig}} = p_{T,assoc} = 0.2 - 2.0$ GeV/c seem to differ from the other results. This is probably due to the ridge elongated along $\Delta\phi$ at $\Delta\eta = 0$, seen in figure 9. The ridge as well as the deviation becomes larger for lower multiplicity classes.

The width of the peak (σ) in both the $\Delta\eta$ and $\Delta\phi$ direction does seem to show a dependence on multiplicity. For lower multiplicities both $\sigma\Delta\eta$ and $\sigma\Delta\phi$ increase. The dependence on multiplicity is strongest for lower momentum ranges, in the higher p_{T} ranges no significant width increase can be observed. These results do not resemble the results of the Pb-Pb study where both the width in $\Delta\eta$ and $\Delta\phi$ were seen to decrease for low multiplicities [5]. However, in both studies the dependence on multiplicity is strongest for $\sigma\Delta\eta$. Furthermore, both studies show that the multiplicity dependence is strongest for lower momentum ranges.

A momentum dependence is observed for both $\sigma\Delta\eta$ and $\sigma\Delta\phi$. In both directions, the width becomes smaller for higher momentum classes. This result was expected and is also found for Pb-Pb collisions. At larger p_{T}, the width becomes smaller since one probes progressively harder processes. This results in particles being contained in a smaller cone for increasing p_{T}.[5]

The jet peak does show circular symmetry in the $\Delta\eta - \Delta\phi$ plane for all p_{T}. This symmetry breaks for lower multiplicity. This has also been observed in other studies of pp collisions [5]. This same study shows that in Pb-Pb collisions, the peak becomes asymmetric for lower multiplicity classes as well as for lower momentum ranges.

The total yield of the near-side peak seems to depend on both momentum and multiplicity. For the low p_{T} ranges, the total yield decreases for lower multiplicity classes. Also, the yield decreases for higher momentum ranges. For higher p_{T} the number of particles that meet this momentum range decreases. Thus, the higher the p_{T} range the less particles are probed. This results in a descrease of the particle yield.

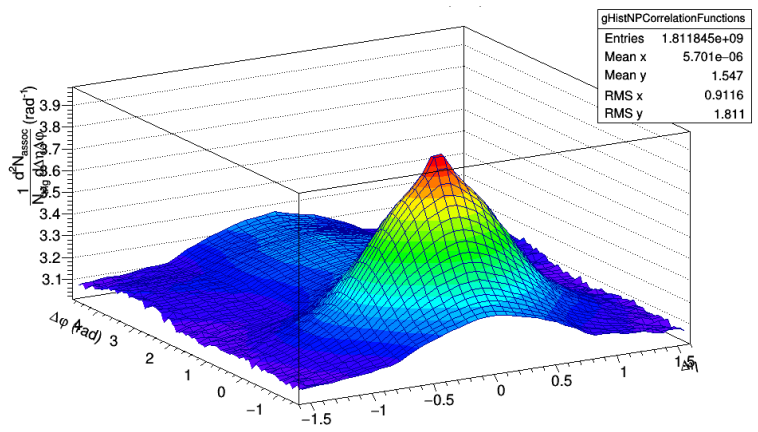

(a) Multiplicity range 0-10%

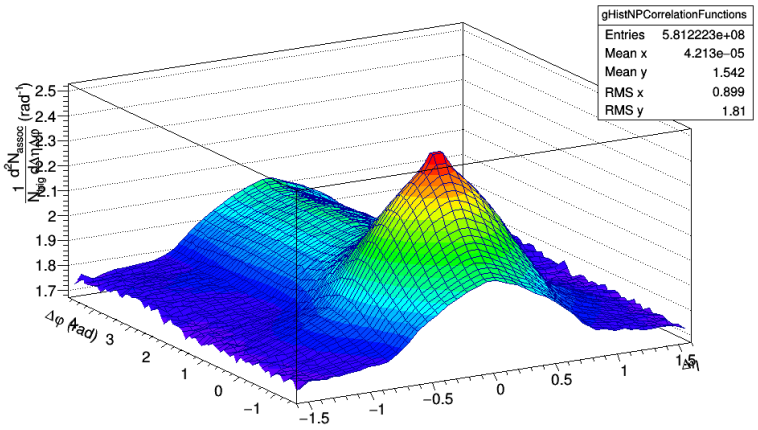

(b) Multiplicity range 30-40%

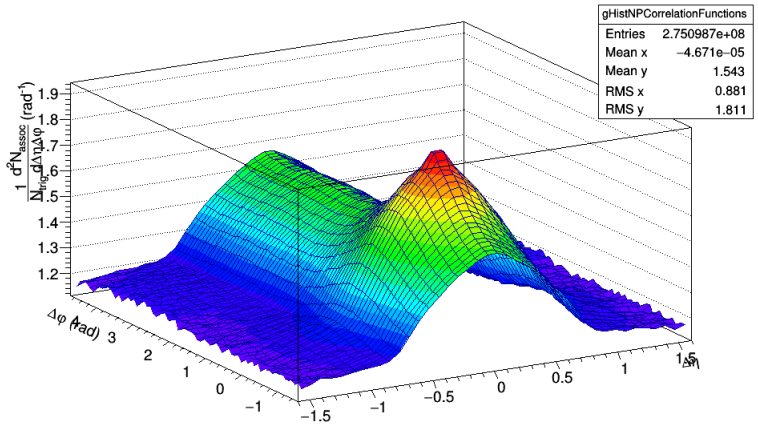

(c) Multiplicity range 60-70%

Figure 9: Yield per trigger particle as a function of $\Delta\phi$ and $\Delta\eta$ in pp collisions at $\sqrt{s_{NN}} = 13$ TeV in three different multiplicity ranges for inclusive sphericity.

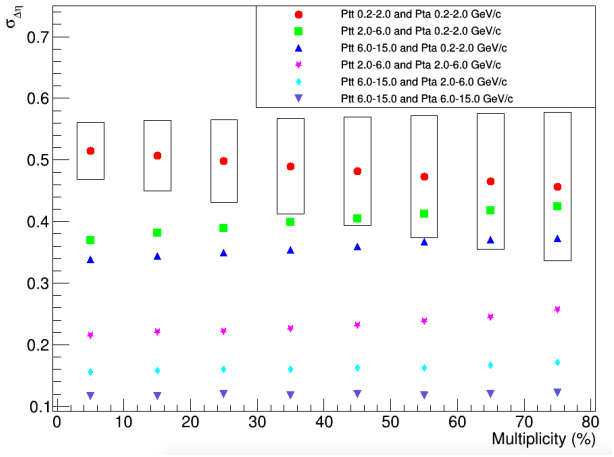

(a) $\sigma\Delta\eta$ calculated using the fit of the projection in $\Delta\eta$.

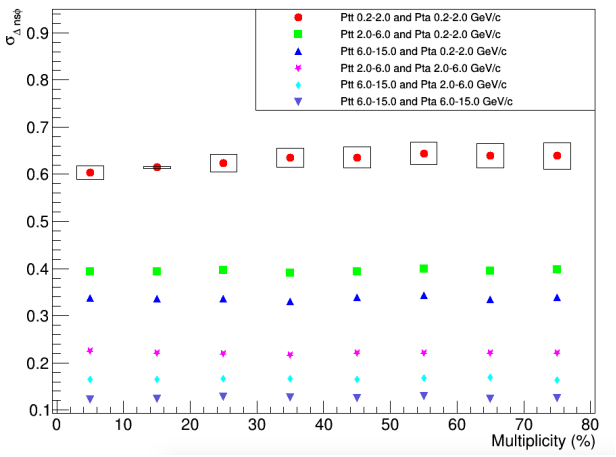

(b) $\sigma\Delta\phi$ calculated using the fit of the projection in $\Delta\phi$.

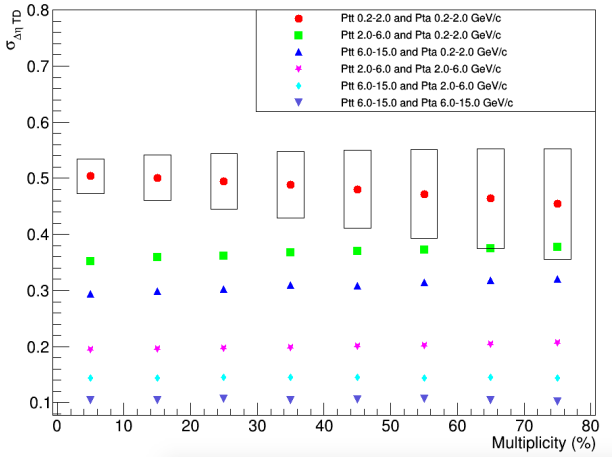

(c) $\sigma\Delta\eta$ calculated using the fit of the two-dimensional histogram .

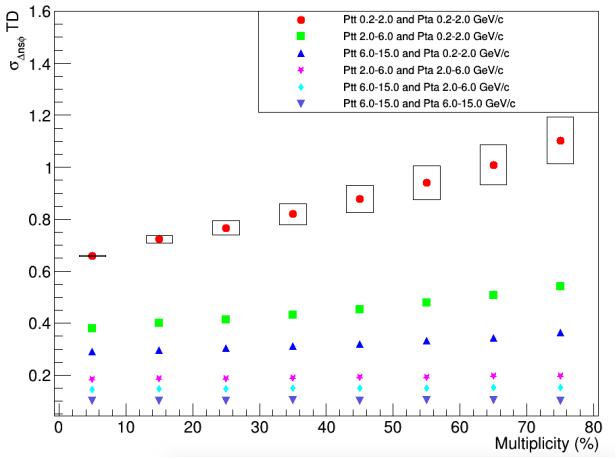

(d) $\sigma\Delta\phi$ calculated using the fit of the two-dimensional histogram .

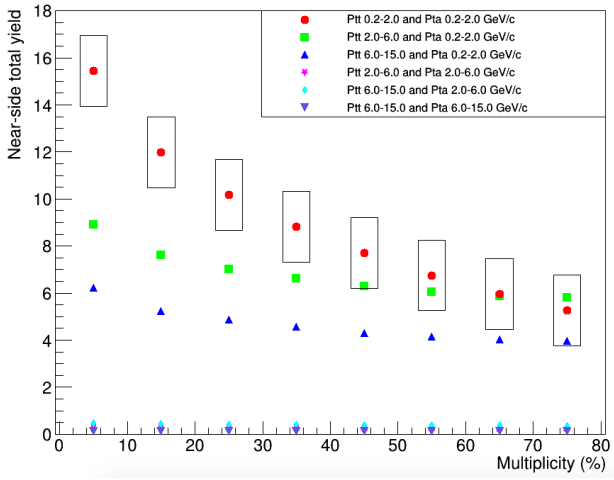

(e) The near-side total yield calculated using the fit of the two-dimensional histogram.

Figure 10: Various fit results for $\sqrt{s_{NN}} = 13$ TeV plotted as a function of multiplicity and momentum.

4.2 Low sphericity

This paragraph includes the results of the low sphericity analysis. In figure 11 the per-trigger yield for momentum range $p_{\mathrm{T,trig}} = 0.2 - 2.0$ GeV/c and $p_{\mathrm{T,assoc}} = 0.2 - 2.0$ GeV/c, and multiplicity ranges 0-10%, 30-40% and 60-70% are presented. The per-trigger yields for higher momentum ranges can be found in appendix B.

The yield per trigger particle for low sphericity differs a lot from inclusive sphericity. For low sphericity, the expected near- and away-side jet peaks are present. Also, the near- and away-side ridges are present. Similarly to results of Pb-Pb collisions, the away-side jet peak dissapears for higher multiplicity indicating the occurence of jet suppression. The away-side jet peak also dissapears for higher momentum ranges. The yield could therefore only be calculated for several momentum and multiplicity ranges.[11]

In figure 12, the yield and shape of the peak for low sphericity are presented. The results for $p_{\mathrm{T,trig}} = p_{\mathrm{T,assoc}} = 0.2 - 2.0$ GeV/c correspond more to the results of the other momentum ranges than for inclusive sphericity. This suggests that for inclusive sphericity the deviation was indeed caused by the ridge elongated along $\Delta\phi$ at $\Delta\eta = 0$.

Again, $\sigma\Delta\eta$ and $\sigma\Delta\phi$ depend on both multiplicity and momentum. As expected, both $\sigma\Delta\eta$ and $\sigma\Delta\phi$ decrease for higher momentum ranges. And again for lower multiplicity, $\sigma\Delta\eta$ and $\sigma\Delta\phi$ increase. However, the width increase is smaller than for inclusive sphericity and there is no significant width dependence on multiplicity for higher momentum ranges.

The near-side total yield also shows the same dependence on multiplicity as for inclusive sphericity, the yield decreases for lower multiplicity. The decrease in yield as a function of multiplicity is stronger for lower momentum ranges.

The momentum dependence for $p_{\mathrm{T,assoc}}$ is also similar to inclusive sphericity, the yield decreases for higher $p_{\mathrm{T,assoc}}$. However, the $p_{\mathrm{T,trig}}$ dependence is different for $p_{\mathrm{T,assoc}} = 2.0 - 6.0$ GeV/c.

Compared to inclusive sphericity, for $p_{\mathrm{T,assoc}} = 0.2 - 2.0$ GeV/c, the values of the near-side total yield are smaller. For $p_{\mathrm{T,assoc}} = 2.0 - 6.0$ GeV/c and $p_{\mathrm{T,assoc}} = 6.0 - 15.0$ GeV/c the values of the yield are similar for both sphericities.

Also, the total yield of the away-side jet peak decreases for lower multiplicity and lower momentum ranges. However, this dependence is probably mainly caused by the amplitude of the ridge due to parton flow. Therefore, we can't conclude that jet quenching is observed.

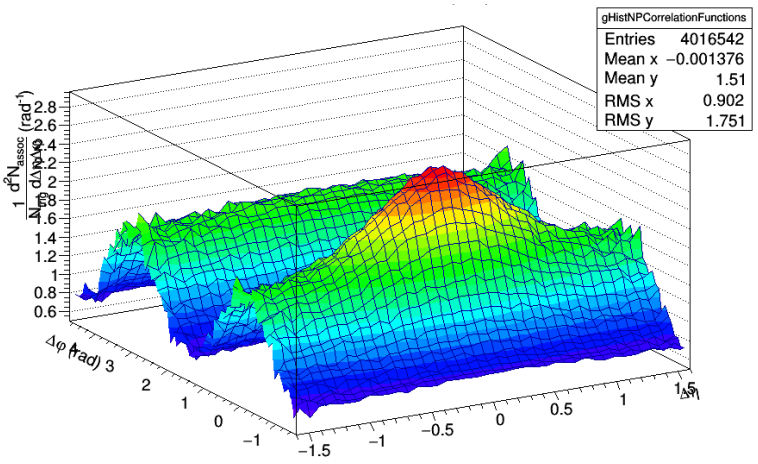

(a) Multiplicity range 0-10%

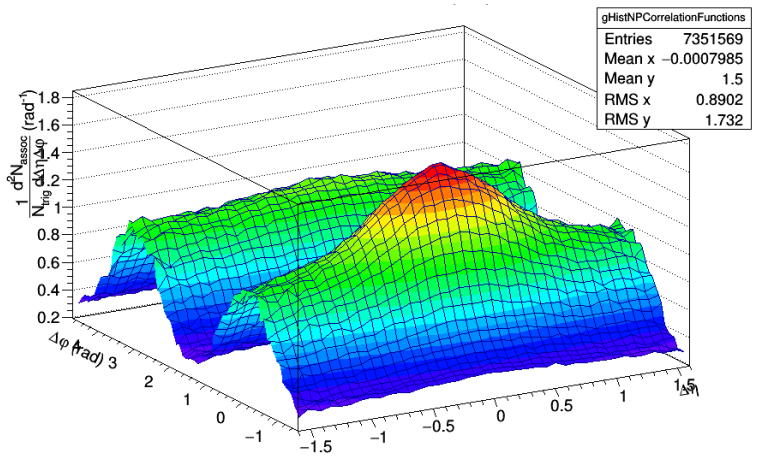

(b) Multiplicity range 30-40%

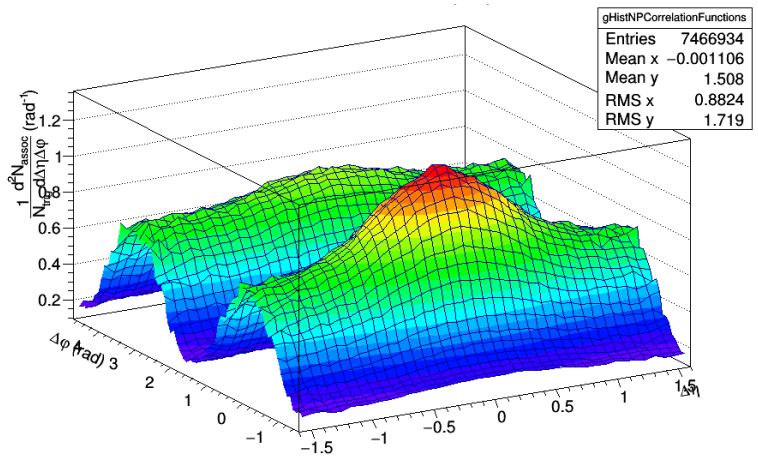

(c) Multiplicity range 60-70%

Figure 11: Yield per trigger particle as a function of $\Delta\phi$ and $\Delta\eta$ in pp collisions at $\sqrt{s_{NN}} = 13$ TeV in three different multiplicity ranges for low sphericity.

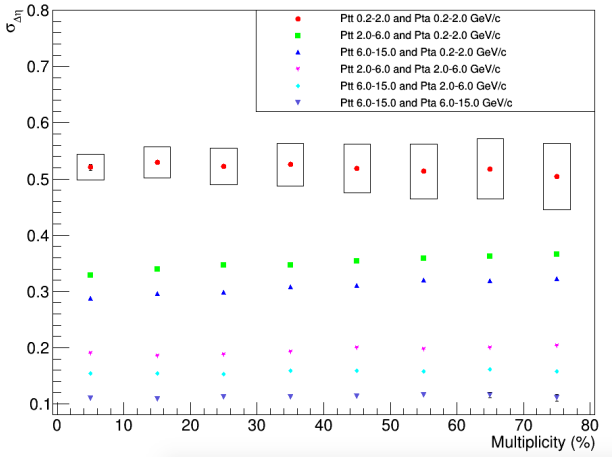

(a) $\sigma\Delta\eta$ calculated using the fit of the projection in $\Delta\eta$.

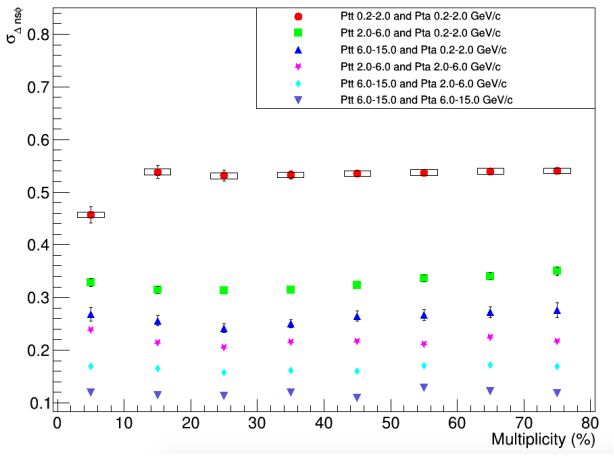

(b) $\sigma\Delta\phi$ calculated using the fit of the projection in $\Delta\phi$.

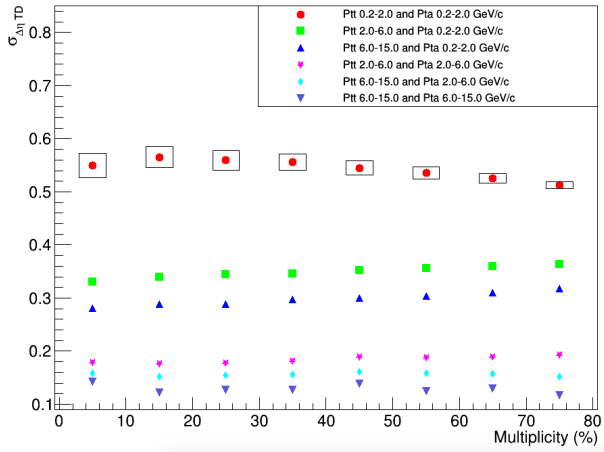

(c) $\sigma\Delta\eta$ calculated using the fit of the two-dimensional histogram .

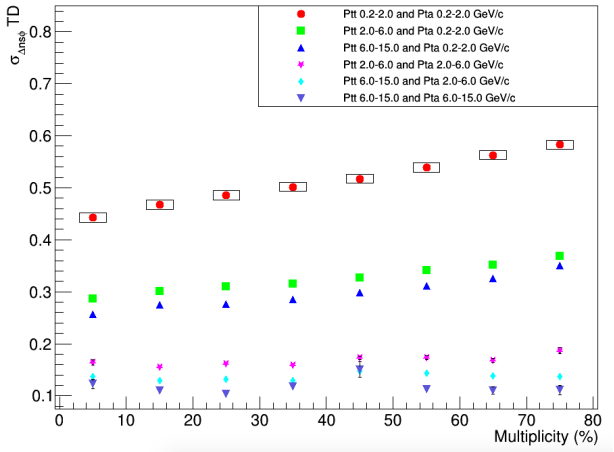

(d) $\sigma\Delta\phi$ calculated using the fit of the two-dimensional histogram .

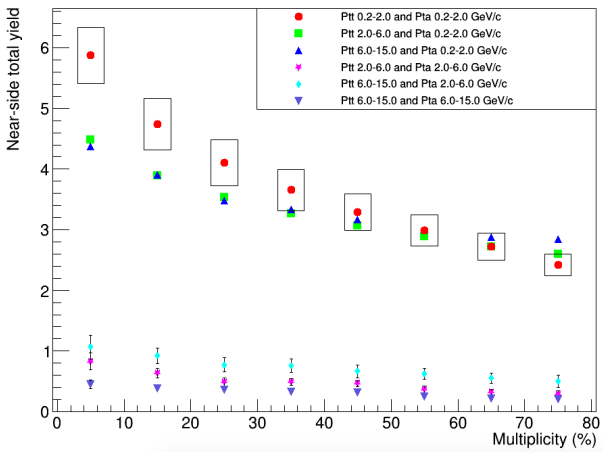

(e) The near-side total yield calculated using the fit of the two-dimensional histogram.

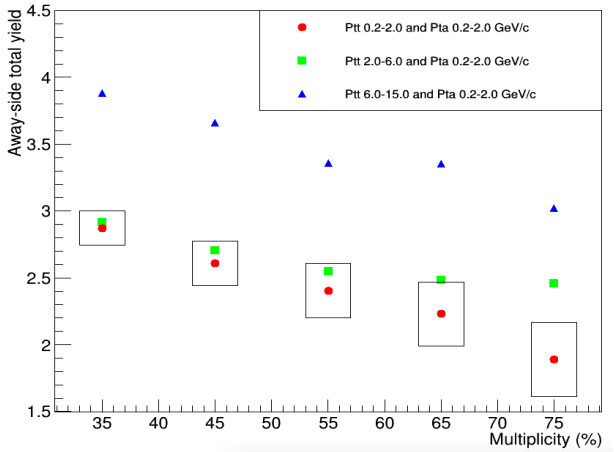

(f) The away-side total yield calculated using the fit of the two-dimensional histogram.

Figure 12: Various fit results for $\sqrt{s_{NN}} = 13$ TeV plotted as a function of multiplicity and momentum for low sphericity.

4.3 Mid sphericity

This paragraph includes the results of the mid sphericity analysis. In figure 13 the per-trigger yields for momentum range $p_{\mathrm{T,trig}} = 0.2 - 2.0$ GeV/c and $p_{\mathrm{T,assoc}} = 0.2 - 2.0$ GeV/c, and multiplicity ranges 0-10%, 30-40% and 60-70% are presented. The per-trigger yields for higher momentum ranges can be found in appendix C.

The yield per trigger particle for mid sphericity does resemble the per-trigger yield for low sphericity. Again, as expected, the near- and away-side jet peaks are present as well as the near- and away-side ridges. Again, the away-side jet peak becomes smaller for higher multiplicities. Additionally, there is a ridge present elongated along $\Delta\phi$ at $\Delta\eta = 0$.

The yield and shape results of the near-side peak are presented in figure 14. Again, the dependence of the width on momentum and multiplicity is similar to inclusive and low sphericity. The width for $p_{\mathrm{T,trig}} = 0.2 - 2.0$ GeV/c and $p_{\mathrm{T,assoc}} = 0.2 - 2.0$ GeV/c, is different from the other results. Similar to the inclusive sphericity, this might be explained by the occurence of the ridge shape elongated along $\Delta\phi$ at $\Delta\eta = 0$.

The results of the total yield for mid sphericity seem to show similar behaviour as the results for inclusive sphericity. Again, the yield decreases for lower multiplicities and higher momentum. However, the values of the yield are lower than for inclusive sphericity and higher than the values for low sphericity. The values for higher momentum ranges are approximately equal as the values for inclusive sphericity and lower than the values for low sphericity. The increase of the values compared to low sphericity might be caused by the ridge elongated along $\Delta\phi$ at $\Delta\eta = 0$.

The results for the total yield of the away-side jet peak are very chaotic. This is probably due to both the away-side ridge due to parton flow together with the ridge elongated along $\Delta\phi$ at $\Delta\eta = 0$. Conclusions about jet suppresion cannot be drawn from these results.

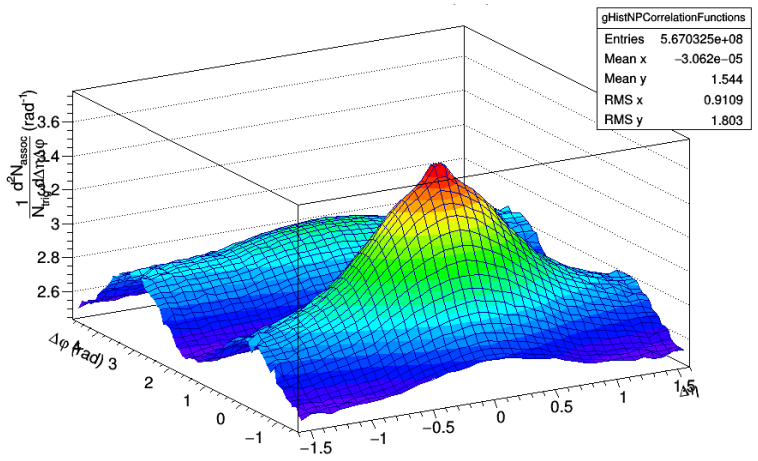

(a) Multiplicity range 0-10%

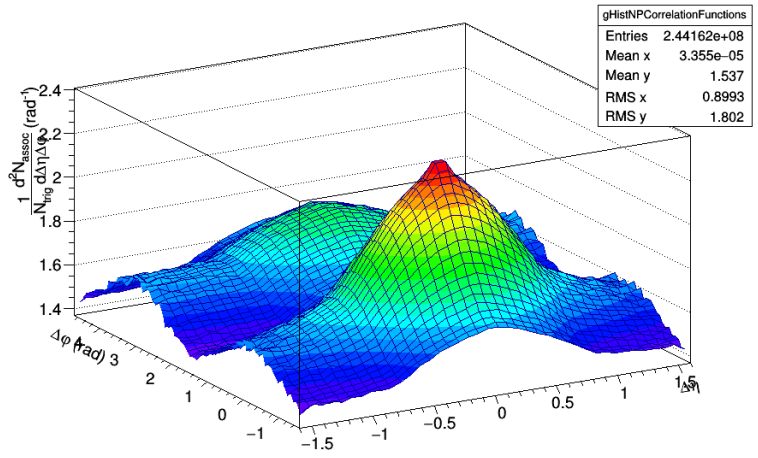

(b) Multiplicity range 30-40%

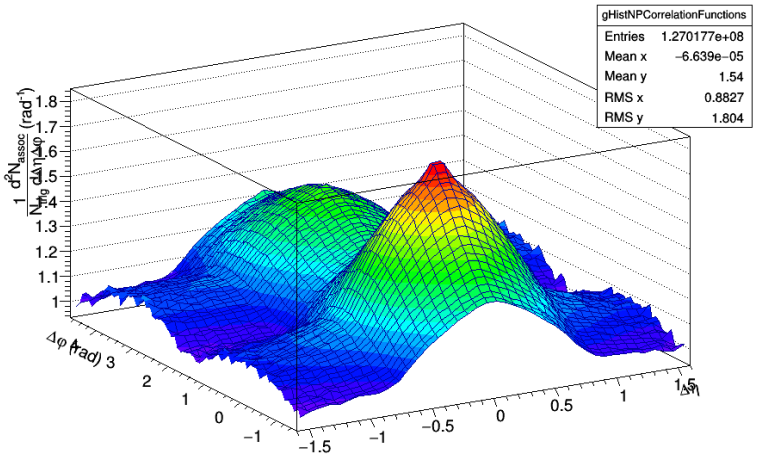

(c) Multiplicity range 60-70%

Figure 13: Yield per trigger particle as a function of $\Delta\phi$ and $\Delta\eta$ in pp collisions at $\sqrt{s_{NN}} = 13$ TeV in three different multiplicity ranges for mid sphericity.

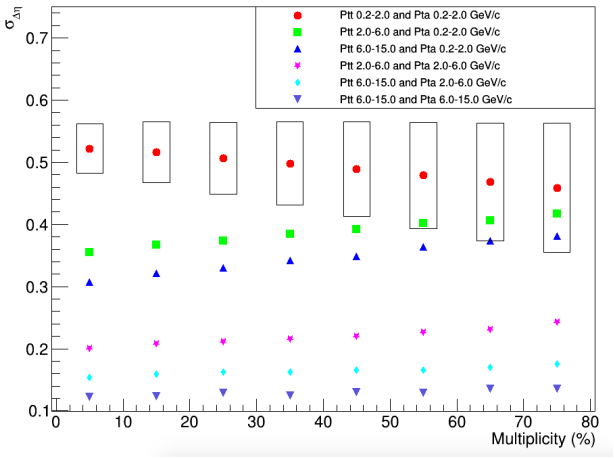

(a) $\sigma\Delta\eta$ calculated using the fit of the projection in $\Delta\eta$.

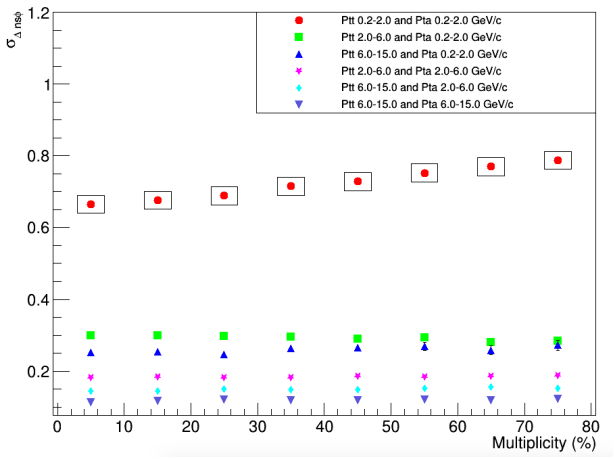

(b) $\sigma\Delta\phi$ calculated using the fit of the projection in $\Delta\phi$.

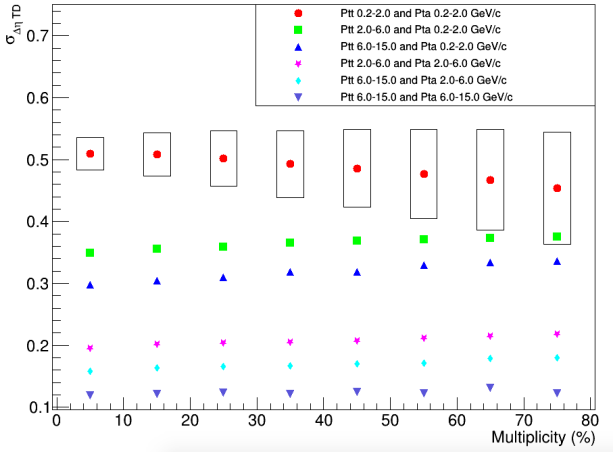

(c) $\sigma\Delta\eta$ calculated using the fit of the two-dimensional histogram .

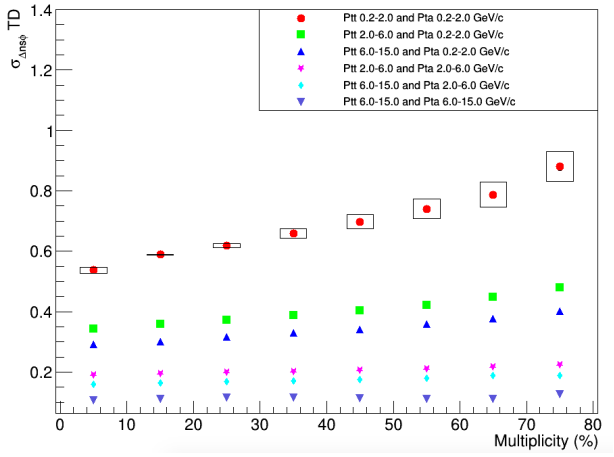

(d) $\sigma\Delta\phi$ calculated using the fit of the two-dimensional histogram .

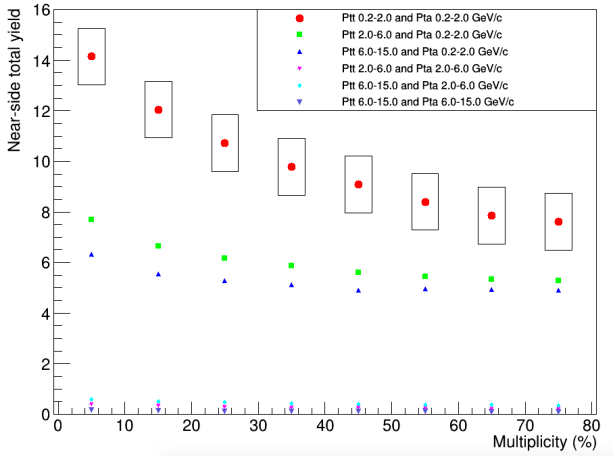

(e) The near-side total yield calculated using the fit of the two-dimensional histogram.

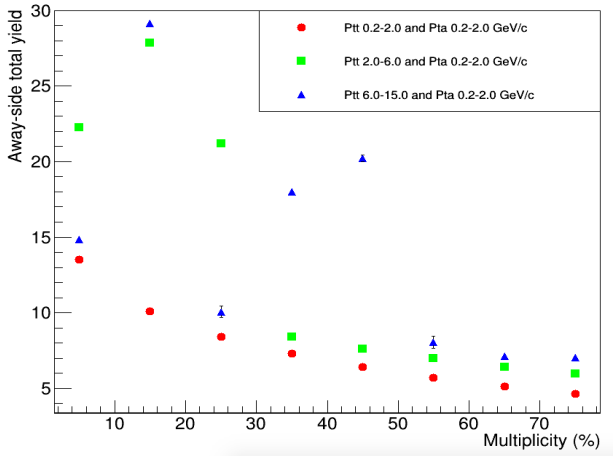

(f) The away-side total yield calculated using the fit of the two-dimensional histogram.

Figure 14: Various fit results for $\sqrt{s_{NN}} = 13$ TeV plotted as a function of multiplicity and momentum for mid sphericity.

4.4 High sphericity

This paragraph includes the results of the inclusive sphericity analysis. In figure 15 the per-trigger yield for lowlow momentum and multiplicity ranges 0-10%, 30-40% and 60-70% are presented. The per-trigger yields for higher momentum ranges can be found in appendix D.

The yield per trigger particle for high sphericity shows similarities and differences compared to the other sphericities. Similarly, the near-side jet peak is visible at $\Delta\phi = \Delta\eta = 0$. However, the away-side jet peak as well as the near- and away-side ridges are not present. Now, the per trigger yield even shows a surpression where the near- and away-side ridges are expected. This indicates why these ridges were not observed for inclusive sphericity. The suppression at high sphericity cancels out the ridges for low and mid sphericity. Similar to mid sphericity, a ridge elongated along $\Delta\phi$ at $\Delta\eta = 0$ is present. For high sphericity this ridge is even higher than for mid sphericity.

Due to the rough behaviour of the yield per trigger particle the plots could not be fitted.

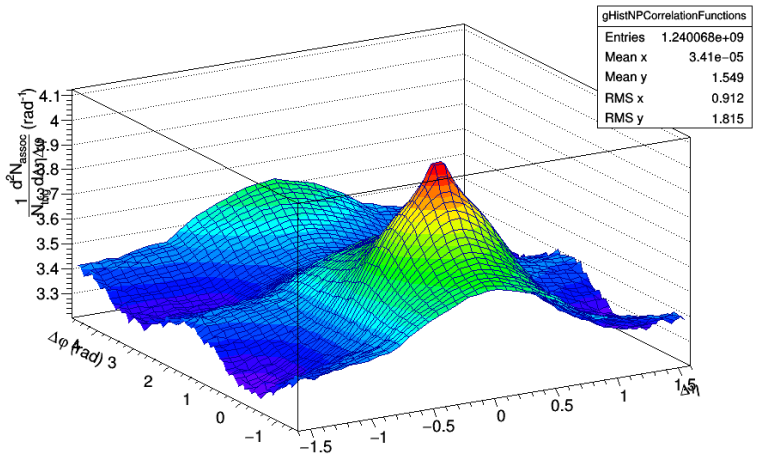

(a) Multiplicity range 0-10%

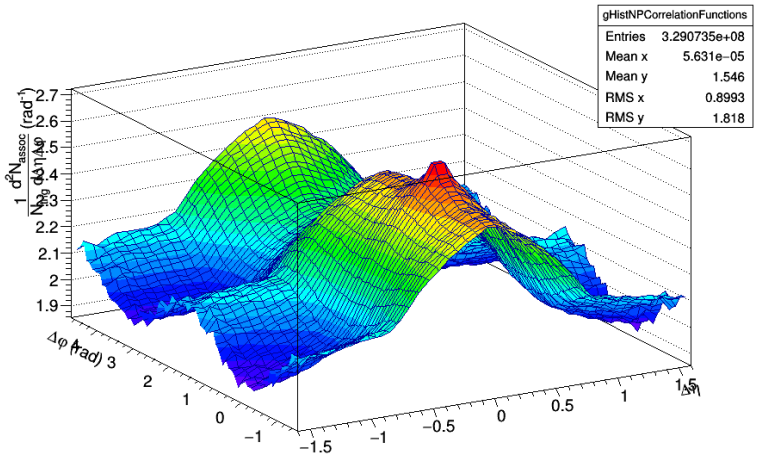

(b) Multiplicity range 30-40%

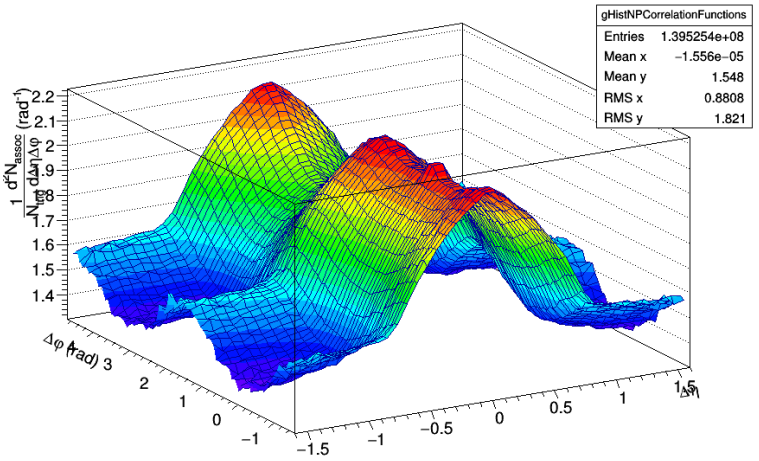

(c) Multiplicity range 60-70%

Figure 15: Yield per trigger particle as a function of $\Delta\phi$ and $\Delta\eta$ in pp collisions at $\sqrt{s_{NN}} = 13$ TeV in three different multiplicity ranges for high sphericity.

4.5 Energy comparison

In this paragraph we present the results of the energy comparison for $\sqrt{s_{NN}} = 5$ TeV and $\sqrt{s_{NN}} = 13$ TeV. The results for the $\sqrt{s_{NN}} = 5$ analysis have been obtained and shared by Nils de Vries. We present the results for inclusive sphericity and $p_{\mathrm{T,trig}} = 0.2 - 2.0$ GeV/c and $p_{\mathrm{T,assoc}} = 0.2 - 2.0$ GeV/c, $p_{\mathrm{T,trig}} = 2.0 - 6.0$ GeV/c and $p_{\mathrm{T,assoc}} = 2.0 - 6.0$ GeV/c and $p_{\mathrm{T,trig}} = 6.0 - 15.0$ GeV/c and $p_{\mathrm{T,assoc}} = 6.0 - 15.0$ GeV/cs. These results can be found in figure 16. We see that the dependencies on momentum and multiplicity are equal for both energies. The size of the jet peak width have equal values for both energies. For the two higher momentum ranges also the size of the total yield for both energies. However, for the low momentum range the total yield is higher for $\sqrt{s_{NN}} = 13$ TeV compared to $\sqrt{s_{NN}} = 5$ TeV.

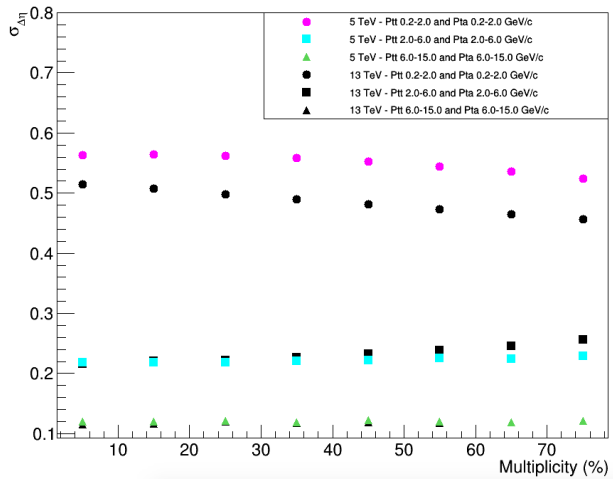

(a) $\sigma\Delta\eta$ calculated using the fit of the projection in $\Delta\eta$ of the two-dimensional histogram.

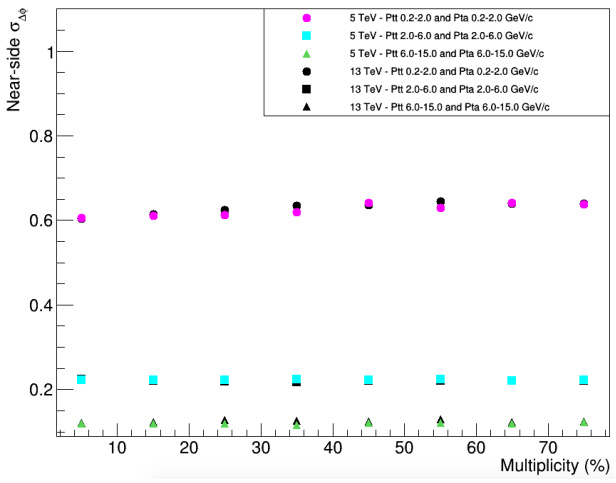

(b) $\sigma\Delta\phi$ calculated using the fit of the projection in $\Delta\phi$ of the two-dimensional histogram.

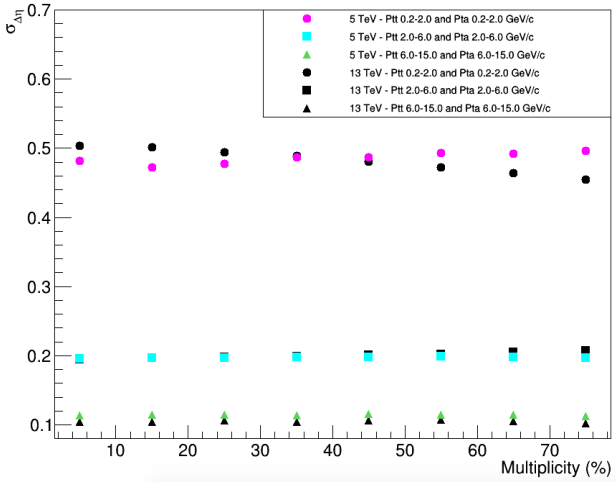

(c) $\sigma\Delta\eta$ calculated using the fit of the two-dimensional histogram .

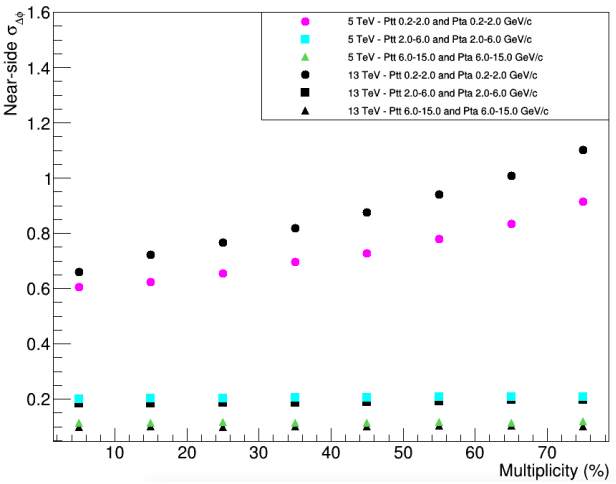

(d) $\sigma\Delta\phi$ calculated using the fit of the two-dimensional histogram .

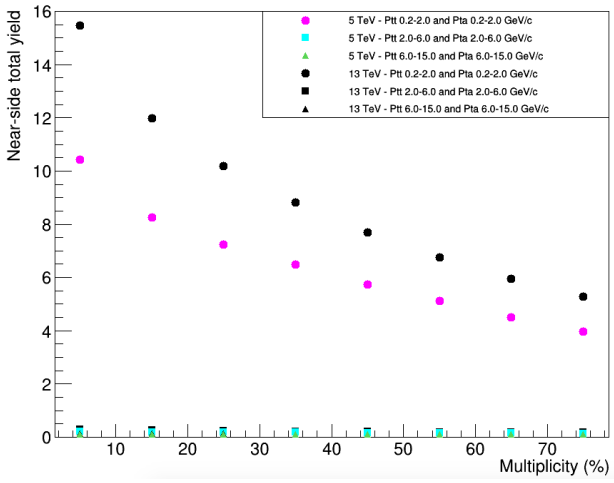

(e) The near-side total yield calculated using the fit of the two-dimensional histogram.

Figure 16: Various fit results compared for $\sqrt{s_{NN}} = 5$ TeV and $\sqrt{s_{NN}} = 13$ TeV plotted as a function of multiplicity and momentum for inclusive sphericity.

5 Conclusions

In this study of pp collisions, several similarities to the study of Pb-Pb collisions are observed. These include the momentum dependence of the width in both the $\Delta\eta$ and $\Delta\phi$ direction, the symmetric shape of the near-side jet peak and the break of this symmetry for lower multiplicities, the presence of the near- and away-side jet peaks as well as ridges for low and mid sphericity, the increase of the total yield for mid sphericity compared to low sphericity and also the suggestion of a shrinking away-side jet peak for higher multiplicities in low and mid sphericity. However, also some differences compared to the Pb-Pb analysis were found. These include the occurence of a ridge elongated along $\Delta\phi$ at $\Delta\eta = 0$, the absence of the away-side peak as well as the absence of the near- and away-side ridges for inclusive sphericity and the increasing width in both the $\Delta\eta$ and $\Delta\phi$ direction for lower multiplicities.

Besides, the results found in this $\sqrt{s_{NN}} = 13$ TeV analysis are very similar to the results found in the $\sqrt{s_{NN}} = 5$ TeV analysis.

6 Discussion and outlook

The statistical errors do not play a large role in this analysis. However, compared to them, the systematic uncertainties are quite large. This implies that the used event and track selection play a large role in the results. The analysis could be improved by using several other criteria for event and track selection and investigate the different results.

Another way to improve the current analysis is by using more sophisticated fit functions including more parameters to describe the signal more adequate. An example would be the fit functions used in [5]. The ridge structures that appeared in the per trigger yield signal influenced the fit of the shape and yield of the jet peak. Therefore, it took quite some time to get these fits right. The spatial limits that where given to the fit function influenced the values of the shape and yield of the jet peak. An improvement for these fit functions would be not only describe the near and away-side ridge but also the ridge elongated along $\Delta\phi$ at $\Delta\eta = 0$.

The phenomena observed in this analysis also provide some suggestions for future research. One could, for example, investigate the origin of the ridge elongated along $\Delta\phi$ at $\Delta\eta = 0$ seen in the yield per trigger particle for mid, high and therefore also inclusive sphericity. Another interesting phenomenon is the appearance of a reduction instead of the near- and away-side ridges in the yield per trigger particle for high sphericity. In this analysis the total yield of the away-side jet peak could not properly be observed due to the presence of signals caused by other phenomena than the back-to-back jet. One could try to develop a technique to distinguish between signals due to flow and signals originating from the jet. This could possibly lead to a better analysis of the total yield of the away-side jet peak, eventually leading to a conclusion wether jet quenching is also observed in pp collisions. By the same means, the signals of the back-to-back jet for high sphericity could be distinguished from background leading to an extinsion of the analysis to high sphericity.

Also, the dependence between the width and the multiplicity, found in this thesis and in the $\sqrt{s}_{\mathrm{NN}} = 5$ TeV analysis, should be further investigated and compared to a model analysis. Also, because the found dependence is not similar to the dependence found in the Pb-Pb analysis [5].

A Per-trigger yield plots for inclusive sphericity

This appendix contains the inclusive sphericity per trigger yield plots for multiple $P_{\mathrm{T,trig}}$ and $P_{\mathrm{T,assoc}}$ ranges.

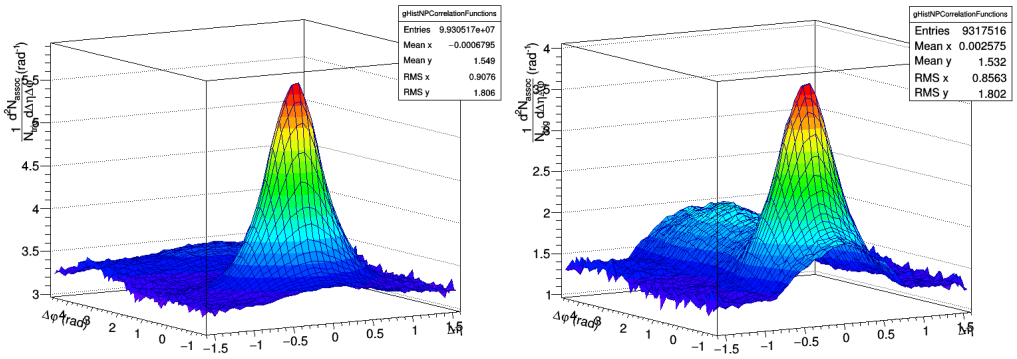

(a) Multiplicity 0-10% (b) Multiplicity 60-70%

Figure 17: Inclusive sphericity per trigger yield for $P_{\mathrm{T,trig}} = 2.0 - 6.0$ GeV/c and $P_{\mathrm{T,assoc}} = 0.2 - 2.0$ GeV/c for high and low multiplicity.

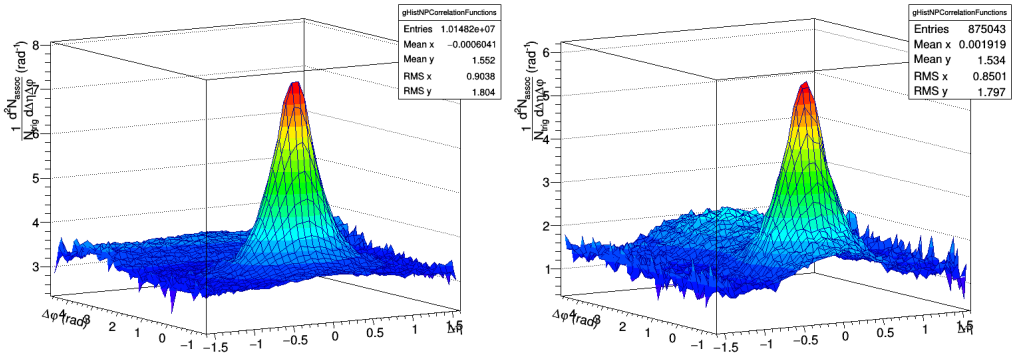

(a) Multiplicity 0-10% (b) Multiplicity 60-70%

Figure 18: Inclusive sphericity per trigger yield for $P_{\mathrm{T,trig}} = 6.0 - 15.0$ GeV/c and $P_{\mathrm{T,assoc}} = 0.2 - 2.0$ GeV/c for high and low multiplicity.

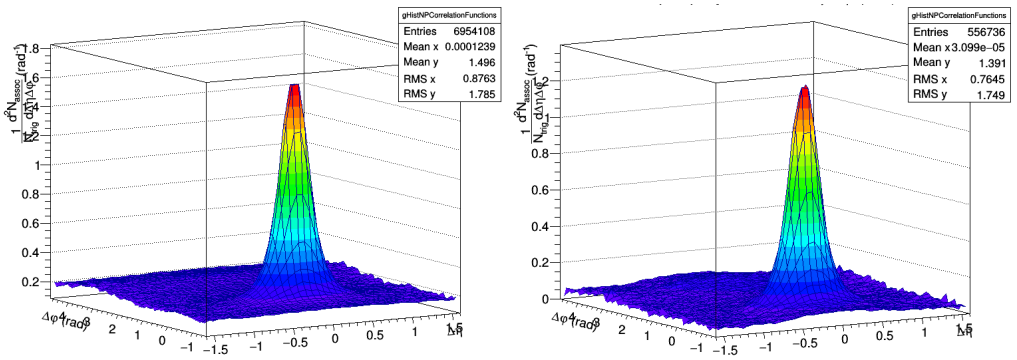

(a) Multiplicity 0-10% (b) Multiplicity 60-70%

Figure 19: Inclusive sphericity per trigger yield for $P_{\mathrm{T,trig}} = 2.0 - 6.0$ GeV/c and $P_{\mathrm{T,assoc}} = 2.0 - 6.0$ GeV/c for high and low multiplicity.

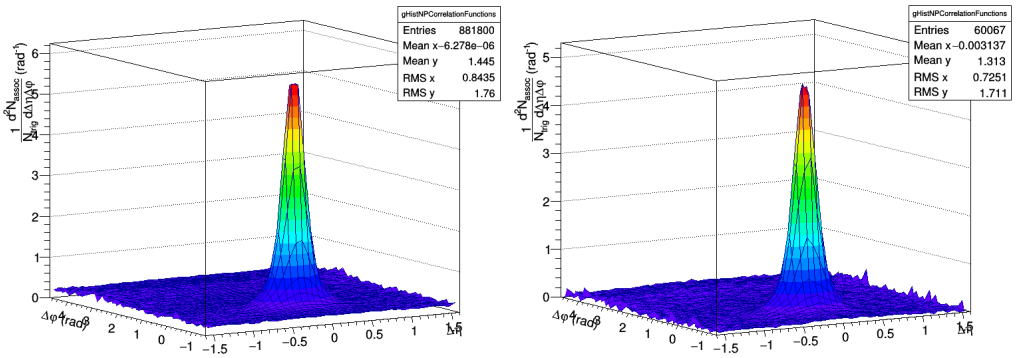

(a) Multiplicity 0-10% (b) Multiplicity 60-70%

Figure 20: Inclusive sphericity per trigger yield for $P_{\mathrm{T,trig}} = 6.0 - 615.0$ GeV/c and $P_{\mathrm{T,assoc}} = 2.0 - 6.0$ GeV/c for high and low multiplicity.

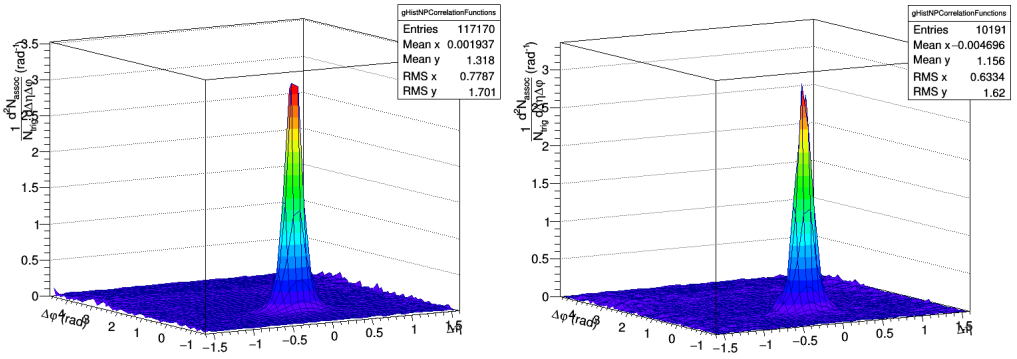

(a) Multiplicity 0-10% (b) Multiplicity 60-70%

Figure 21: Inclusive sphericity per trigger yield for $P_{\mathrm{T,trig}} = 6.0 - 15.0$ GeV/c and $P_{\mathrm{T,assoc}} = 6.0 - 15.0$ GeV/c for high and low multiplicity.

B Per-trigger yield plots for low sphericity

This appendix contains the low sphericity per trigger yield plots for multiple multiplicity ranges and $P_{\mathrm{T,trig}}$ and $P_{\mathrm{T,assoc}}$ ranges.

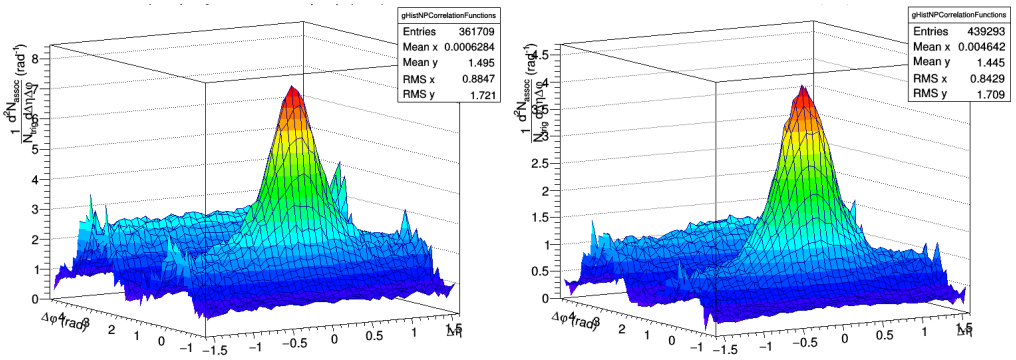

(a) Multiplicity 0-10% (b) Multiplicity 60-70%

Figure 22: Low sphericity per trigger yield for $P_{\mathrm{T,trig}} = 2.0 - 6.0$ GeV/c and $P_{\mathrm{T,assoc}} = 0.2 - 2.0$ GeV/c for high and low multiplicity.

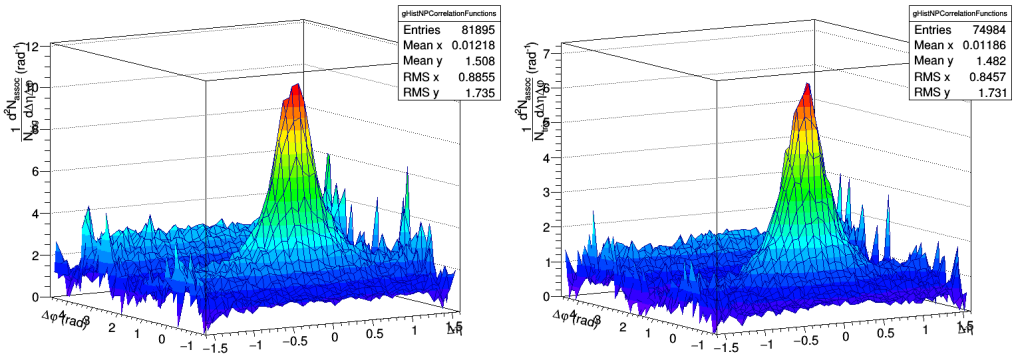

(a) Multiplicity 0-10% (b) Multiplicity 60-70%

Figure 23: Low sphericity per trigger yield for $P_{\mathrm{T,trig}} = 6.0 - 15.0$ GeV/c and $P_{\mathrm{T,assoc}} = 0.2 - 2.0$ GeV/c for high and low multiplicity.

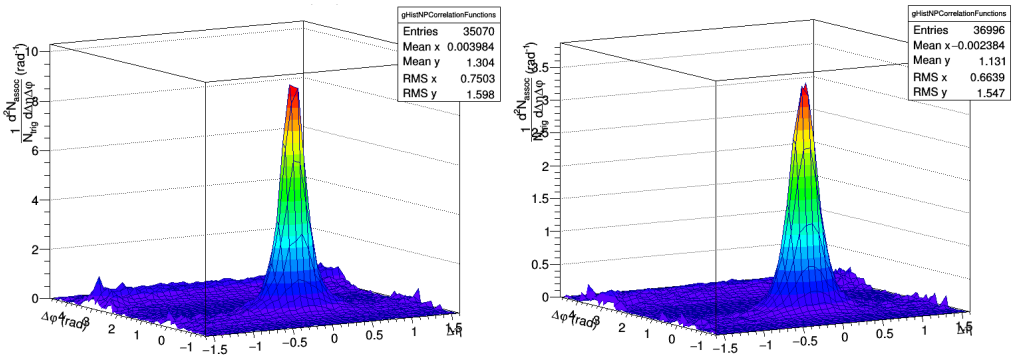

(a) Multiplicity 0-10% (b) Multiplicity 60-70%

Figure 24: Low sphericity per trigger yield for $P_{\mathrm{T,trig}} = 2.0 - 6.0$ GeV/c and $P_{\mathrm{T,assoc}} = 2.0 - 6.0$ GeV/c for high and low multiplicity.

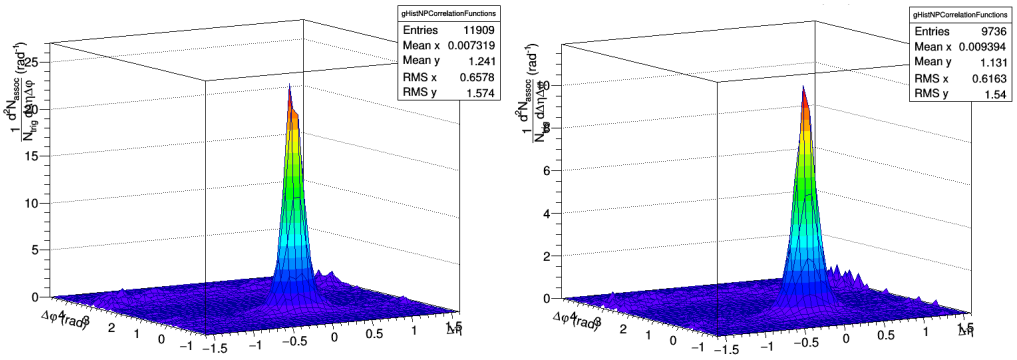

(a) Multiplicity 0-10% (b) Multiplicity 60-70%

Figure 25: Low sphericity per trigger yield for $P_{\mathrm{T,trig}} = 6.0 - 615.0$ GeV/c and $P_{\mathrm{T,assoc}} = 2.0 - 6.0$ GeV/c for high and low multiplicity.

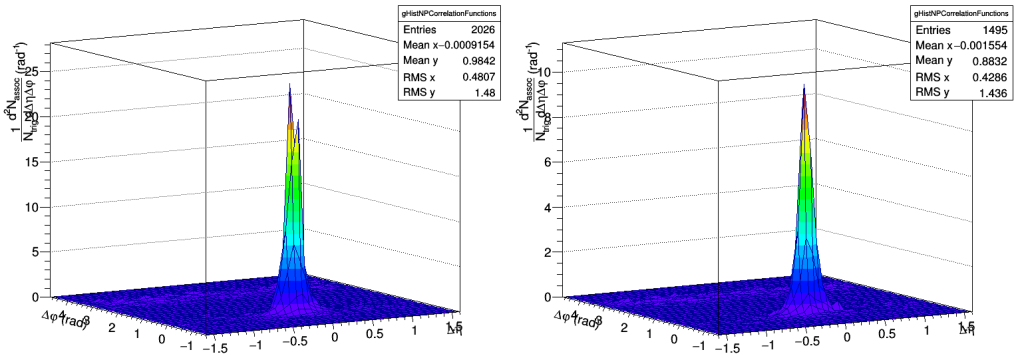

(a) Multiplicity 0-10% (b) Multiplicity 60-70%

Figure 26: Low sphericity per trigger yield for $P_{\mathrm{T,trig}} = 6.0 - 15.0$ GeV/c and $P_{\mathrm{T,assoc}} = 6.0 - 15.0$ GeV/c for high and low multiplicity.

C Per-trigger yield plots for mid sphericity

This appendix contains the mid sphericity per trigger yield plots for multiple multiplicity ranges and $P_{\mathrm{T,trig}}$ and $P_{\mathrm{T,assoc}}$ ranges.

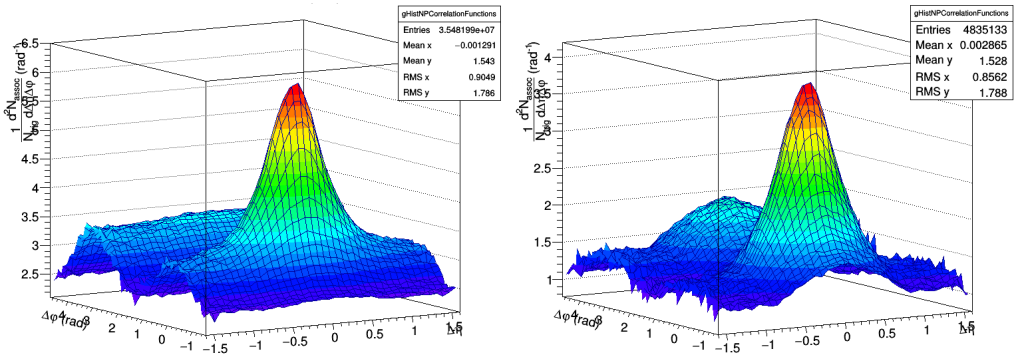

(a) Multiplicity 0-10% (b) Multiplicity 60-70%

Figure 27: Mid sphericity per trigger yield for $P_{\mathrm{T,trig}} = 2.0 - 6.0$ GeV/c and $P_{\mathrm{T,assoc}} = 0.2 - 2.0$ GeV/c for high and low multiplicity.

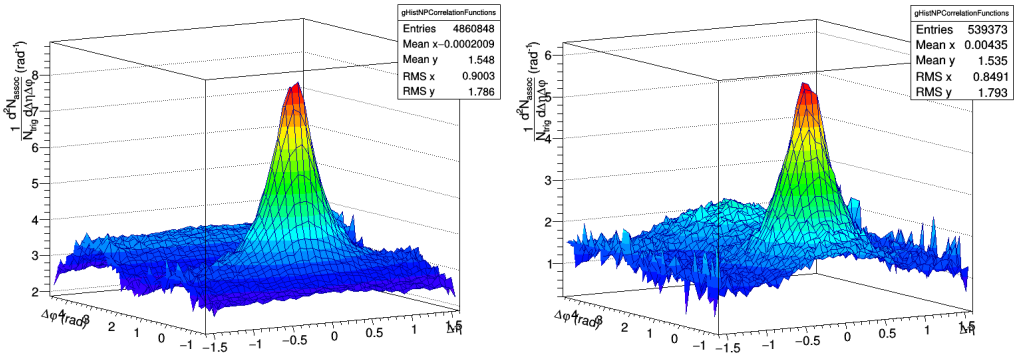

(a) Multiplicity 0-10% (b) Multiplicity 60-70%

Figure 28: Mid sphericity per trigger yield for $P_{\mathrm{T,trig}} = 6.0 - 15.0$ GeV/c and $P_{\mathrm{T,assoc}} = 0.2 - 2.0$ GeV/c for high and low multiplicity.

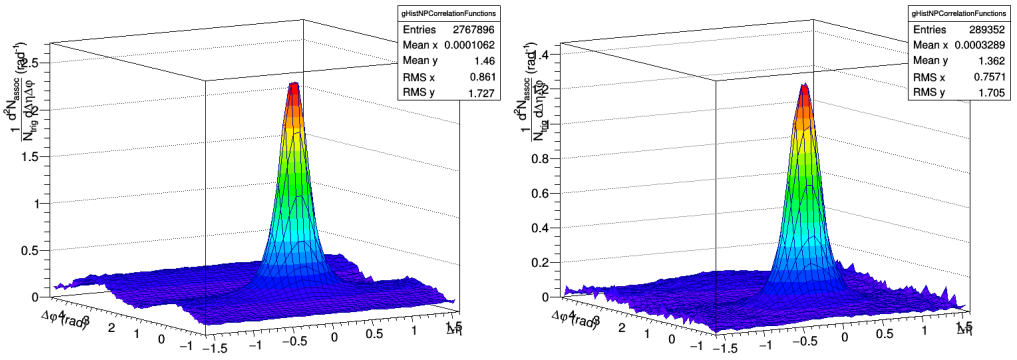

(a) Multiplicity 0-10% (b) Multiplicity 60-70%

Figure 29: Mid sphericity per trigger yield for $P_{\mathrm{T,trig}} = 2.0 - 6.0$ GeV/c and $P_{\mathrm{T,assoc}} = 2.0 - 6.0$ GeV/c for high and low multiplicity.

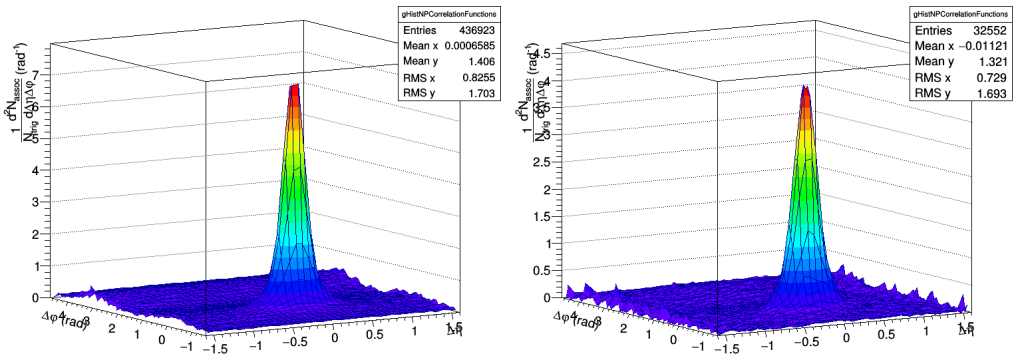

(a) Multiplicity 0-10% (b) Multiplicity 60-70%

Figure 30: Mid sphericity per trigger yield for $P_{\mathrm{T,trig}} = 6.0 - 15.0$ GeV/c and $P_{\mathrm{T,assoc}} = 2.0 - 6.0$ GeV/c for high and low multiplicity.

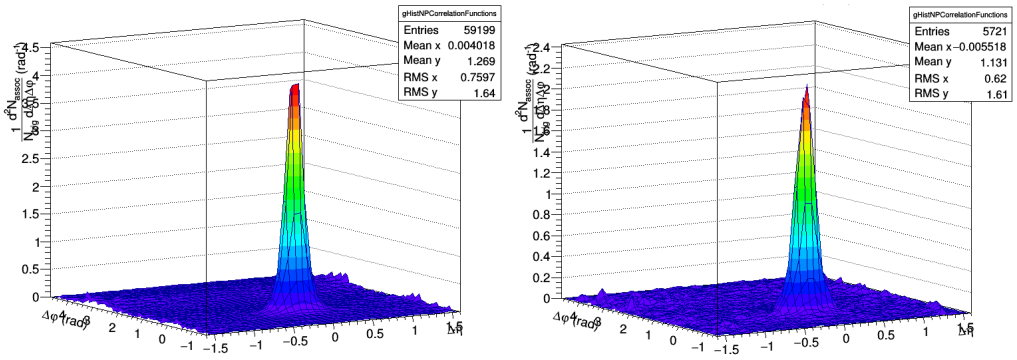

(a) Multiplicity 0-10% (b) Multiplicity 60-70%

Figure 31: Mid sphericity per trigger yield for $P_{\mathrm{T,trig}} = 6.0 - 15.0$ GeV/c and $P_{\mathrm{T,assoc}} = 6.0 - 15.0$ GeV/c for high and low multiplicity.

D Per-trigger yield plots for high sphericity

This appendix contains the high sphericity per trigger yield plots for multiple multiplicity ranges and $P_{\mathrm{T,trig}}$ and $P_{\mathrm{T,assoc}}$ ranges.

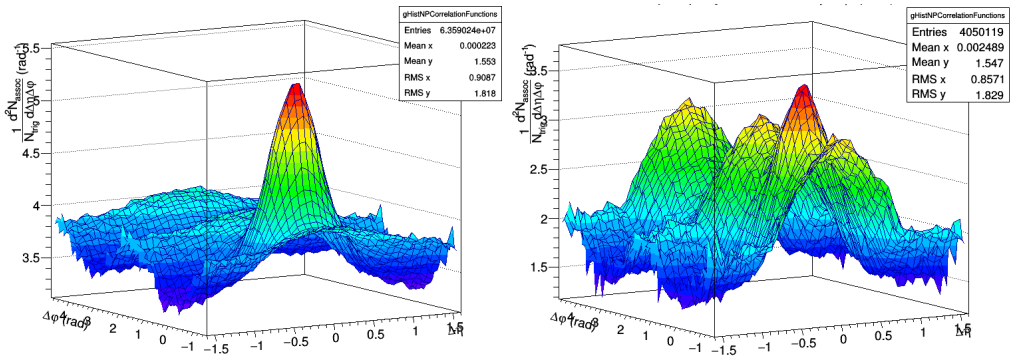

(a) Multiplicity 0-10% (b) Multiplicity 60-70%

Figure 32: High sphericity per trigger yield for $P_{\mathrm{T,trig}} = 2.0 - 6.0$ GeV/c and $P_{\mathrm{T,assoc}} = 0.2 - 2.0$ GeV/c for high and low multiplicity.

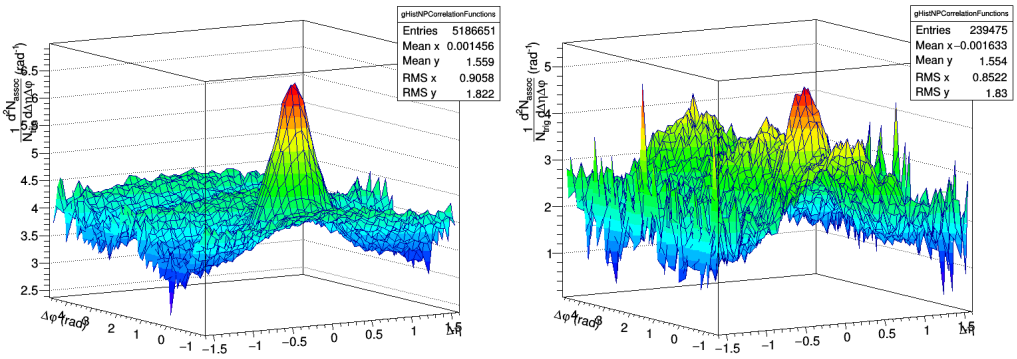

(a) Multiplicity 0-10% (b) Multiplicity 60-70%

Figure 33: High sphericity per trigger yield for $P_{\mathrm{T,trig}} = 6.0 - 15.0$ GeV/c and $P_{\mathrm{T,assoc}} = 0.2 - 2.0$ GeV/c for high and low multiplicity.

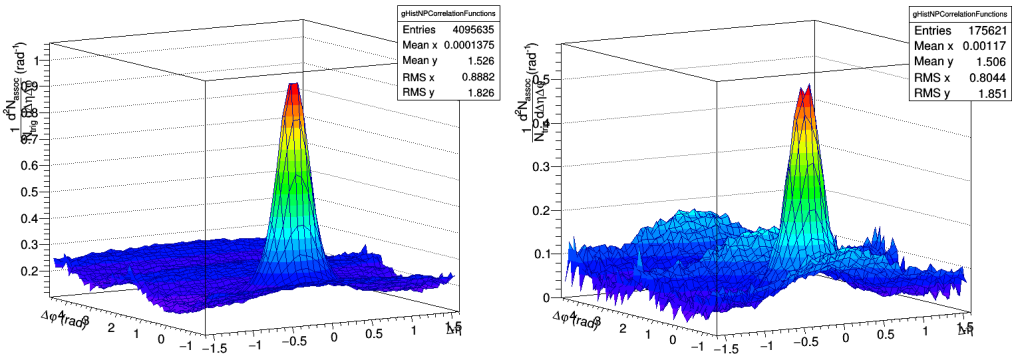

(a) Multiplicity 0-10% (b) Multiplicity 60-70%

Figure 34: High sphericity per trigger yield for $P_{\mathrm{T,trig}} = 2.0 - 6.0$ GeV/c and $P_{\mathrm{T,assoc}} = 2.0 - 6.0$ GeV/c for high and low multiplicity.

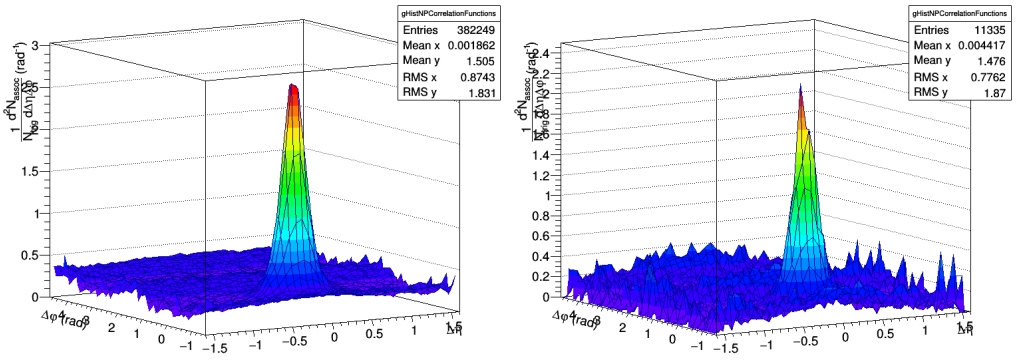

(a) Multiplicity 0-10% (b) Multiplicity 60-70%

Figure 35: High sphericity per trigger yield for $P_{\mathrm{T,trig}} = 6.0 - 615.0$ GeV/c and $P_{\mathrm{T,assoc}} = 2.0 - 6.0$ GeV/c for high and low multiplicity.

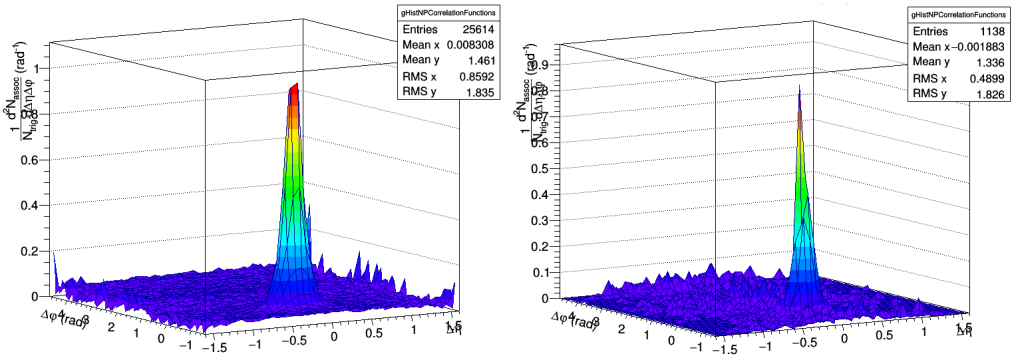

(a) Multiplicity 0-10% (b) Multiplicity 60-70%

Figure 36: High sphericity per trigger yield for $P_{\mathrm{T,trig}} = 6.0 - 15.0$ GeV/c and $P_{\mathrm{T,assoc}} = 6.0 - 15.0$ GeV/c for high and low multiplicity.

References

[1] K. et al. (ALICE Collaboration) Aamodt. "The ALICE experiment at the CERN LHC". In: *Journal of Instrumentation* 3.08 (2008), S08002.

[2] B. et al. (ALICE Collaboration) Abelev. "Transverse sphericity of primary charged particles in minimum bias proton–proton collisions at $\sqrt{s} = 0.9, 2.76$ and 7 TeV". In: *The European Physical Journal C* 72.9 (2012), p. 2124.

[3] S. et al. (ALICE Collaboration) Acharya. "Investigations of anisotropic flow using multi-particle azimuthal correlations in pp, p-Pb, Xe-Xe, and Pb-Pb collisions at the LHC". In: *arXiv preprint arXiv:1903.01790* (2019).

[4] S. et al. (ALICE Collaboration) Acharya. "Measurement of D-meson production at mid-rapidity in pp collisions at $\sqrt{s} = 7$ TeV". In: *The European Physical Journal C* 77.8 (2017), p. 550.

[5] J. et al. (ALICE Collaboration) Adam. "Anomalous Evolution of the Near-Side Jet Peak Shape in Pb-Pb Collisions at s N N= 2.76 TeV". In: *Physical review letters* 119.10 (2017), p. 102301.

[6] J. et al. (ALICE Collaboration) Adam. "Pseudorapidity and transverse-momentum distributions of charged particles in proton-proton collisions at $\sqrt{s} = 13$ TeV". In: *arXiv preprint arXiv:1509.08734* (2015).

[7] ALICE Collaboration. *The ALICE experiment*. `http://aliceinfo.cern.ch/Public/en/Chapter2/Chap2InsideAlice-en.html`. 2008.

[8] Y et al. Aoki. "The order of the quantum chromodynamics transition predicted by the standard model of particle physics". In: *Nature* 443.7112 (2006), p. 675.

[9] P. Braun-Munzinger and J. Stachel. "The quest for the quark–gluon plasma". In: *Nature* 448.7151 (2007), p. 302.

[10] M. et al. Connors. "Review of jet measurements in heavy ion collisions". In: *arXiv preprint arXiv:1705.01974* (2017).

[11] U. W. Heinz. "Concepts of heavy-ion physics". In: *arXiv preprint hep-ph/0407360* (2004).

[12] T. Hülsing. *Probing quantum chromodynamics with the ATLAS detector: charged-particle event shape variables and the dijet cross-section*. Tech. rep. 2014.

[13] B. R. Martin. *Nuclear and particle physics: an introduction*. Wiley, 2019.

[14] A. Ortiz. "Experimental results on event shapes at hadron colliders". In: *arXiv preprint arXiv:1705.02056* (2017).

[15] M. Veldhoen. "Identified particle yield associated with a high-pT trigger particle at the LHC". PhD thesis. Utrecht University, 2016.